Wavelet Modulation in Gaussian and Rayleigh Fading Channels

Manish J. Manglani

Thesis submitted to the Faculty of the
Virginia Polytechnic Institute and State University
(Virginia Tech)
in partial fulfillment of the requirements for the degree of

Master of Science
in
Electrical Engineering

Dr. Amy E. Bell, Chair
Dr. Ira Jacobs
Dr. Brian D. Woerner

July, 2001
Blacksburg, Virginia

Keywords: Wavelet Modulation, Wavelets, Fractal Modulation
AWGN channel, Flat Fading, Frequency Selective Fading

Wavelet Modulation in Gaussian and Rayleigh Fading Channels

Manish J. Manglani

(ABSTRACT)

Wavelet Modulation (WM)—also referred to as fractal modulation—simultaneously sends data at multiple rates through an unknown channel. This novel multirate diversity strategy offers improved message recovery over conventional modulation techniques: if the message is not received at one rate due to the channel disturbances, it can be received at another rate where the channel is clear. Previous research has demonstrated the performance of wavelet modulation in Gaussian channels.

This thesis extends the investigation to the performance of wavelet modulation in time varying channels. We show that bit error rate (BER) wavelet demodulation performance in the additive, white, Gaussian noise (AWGN) channel is comparable to theoretical binary phase shift keying. These wavelet modulation results in the AWGN channel are better at every signal to noise ratio (SNR) than in either of the two Rayleigh, flat, slow fading channels and the two frequency selective, slow fading channels that we tested. Our results depict the improvement in performance that can be realized for time varying channels by utilizing the various rates of wavelet modulation; BER versus SNR curves for each fading channel show how the message at one rate can be more accurately recovered than at another rate. Furthermore, we also present results indicating the dramatic improvement in wavelet demodulation performance when multiple rates are available and utilized for demodulation. This improvement in performance is highly visible in BER performance for the AWGN and flat fading channels.

Finally, a comparision of binary phase shift keying (BPSK) and WM in a frequency selective channel is performed. The BER improvement of WM is shown when demodulation is done at rates which are least corrupted by ISI. We illustrate our new algorithm that: identifies the

channel characteristics; determines which rates are maximally corrupted by ISI; and, utilizes only those uncorrupted copies in demodulation.

Acknowledgments

I am very thankful to my advisor Dr. Amy Bell for the guidance and support given to me by her during the pursuit of my Master's degree at Virginia Tech. She has been very helpful and I could always turn to her for assistance when the obstacles appeared insurmountable. I am grateful for her willingness and readiness in giving direction to our research work.

I would like to thank Dr. Brian Woerner for his invaluable ideas and suggestions during the course of my research work. I would also like to thank Dr. Ira Jacobs for readily agreeing to be on my committee and evaluating the thesis.

I am also grateful for the support and help provided by my colleagues Lakshmi Iyer and Andy Beegan. They were always ready to take out time and provide helpful suggestions.

Last, but not least, I would like to thank my family who were a source of constant support and encouragement.

Contents

List of Figures

List of Tables

Chapter 1

Introduction

1.1 Motivation

A promising application of wavelet transforms is in the field of digital wireless communications where they can be used to generate waveforms that are suitable for transmission over wireless channels. This type of modulation is known as wavelet modulation (WM) or fractal modulation. The advantage of this scheme emerges from its diversity strategy: wavelet modulation allows transmission of the data signal at multiple rates simultaneously. This multirate diversity scheme offers advantages in mobile communications where multipath and Doppler fading effects may introduce severe distortion. If the data at a particular rate (i.e. scale or frequency) is corrupted by intersymbol interference (ISI)—or some other form of distortion—the redundant data at another rate can be used for demodulation at the receiver.

This thesis investigates three aspects of WM. First, the performance of WM in 3 different types of channels is investigated and compared to binary phase shift keying (BPSK). Second, the performance of WM using a joint statistic is evaluated; this is an estimate of the

transmitted symbol that is calculated using two or more noisy observations. And third, a method to detect the channel type is illustrated. This technique also performs ISI excision and results in improved performance in frequency-selective channels.

1.2 Previous Related Research

Wornell and Oppenheim outlined the design of the transmitter and receiver for WM [19]. The performance of WM in an additive, white Gaussian noise (AWGN) channel was also evaluated in Wornell's work [19]. Wornell showed that the bit error rate (BER) performance of WM is a function of SNR in the channel; the estimate of the received bit becomes more accurate as the number of noisy observations used to calculate it is increased. Ptasinski and Fellman simulated WM using the Daubechies $N = 4$ wavelet and measured its BER performance in an AWGN channel [10]. Ptasinski's work showed the performance of WM to be equivalent to that calculated by Wornell (i.e. the results were equivalent to BPSK performance for the AWGN channel) [10]. These results are summarized in more detail in Chapter 3, Section 3.5. In all of the previous research, the BER performance was measured using a single scale (i.e. rate) for demodulation.

Wavelets have also been proposed for use in other aspects of communication systems. Multiple access schemes using orthogonal wavelet-based codes have been proposed as an alternative to code division multiple access (CDMA) [2, 20]. Wavelet-based modulation techniques for frequency-hopped spread spectrum communications have also appeared in the literature [3, 13]. The wavelet packet transform—an extension of the wavelet transform in which the highpass branches are iterated as well as the lowpass branches—has led to the development of wavelet packet modulation (WPM). This modulation technique exploits the larger selection of time-frequency tilings at its disposal to minimize channel disturbances [8, 17].

1.3 Significance of this Research

We explore the performance of WM in 3 channel types: AWGN, flat fading and frequency-selective fading. WM research to date has not explored its performance in Rayleigh fading channels; by investigating WM performance in fading channels, we attempt to show the suitability of this scheme for a mobile radio environment. For AWGN channels, the simulated results match the theoretical results calculated by Wornell [19].

Furthermore, joint estimation techniques have been simulated at the receiver for the AWGN, the Rayleigh flat fading and the frequency-selective fading channels. The results show significant improvements in error rate as the number of observations used to calculate the statistic is increased. For example, in the AWGN channel when the number of noisy observations is increased from 1 to 2, a 3.8dB performance gain is realized.

In addition, a method to determine the type of channel is presented. This method allows the receiver to determine the type of channel present between the transmitter and itself. In the frequency-selective channel, one or more scales may be corrupted while data at other scales may not be adversely affected by ISI. Our method detects the corrupted scales and throws away this data. We illustrate the resulting bit error rate performance of WM and show its superiority over BPSK.

This thesis provides the following new results.

- Bit error rate performance of WM as a function of SNR in AWGN, Rayleigh flat fading and frequency selective fading channels. The performance of WM is also compared to BPSK in each of these channels.
- A novel joint statistic is developed for the receiver for the AWGN, the Rayleigh flat fading and the frequency-selective fading channels. Experimental results indicate an improved BER performance in AWGN and flat fading channels.

- A new statistical method is developed to classify the channel as either: AWGN, flat fading or frequency-selective.
- For the frequency-selective channel, a novel method is described to detect and discard ISI corrupted scales—thus improving BER performance.

1.4 Outline of this Thesis

This thesis is organized as follows. Chapter 2 describes the three channels used in our investigation of WM bit error rate performance. Chapter 3 presents an overview of the discrete wavelet transform (DWT) and the basic concepts of wavelet modulation. This chapter also describes several implementation issues involved in the simulation of WM. Chapter 4 illustrates two new methods: (1) computation of a joint statistic, and (2) channel detection and ISI excision (in frequency-selective channels). Chapter 5 illustrates the performance of WM for the three channels used in the simulations. It also shows the improved results obtained using the new joint statistic technique. Improved results using the channel detection algorithm and removal of corrupted scales is also described. Chapter 6 concludes the thesis and suggests directions for future work.

Chapter 2

Channel Models

In this thesis, the performance of WM has been examined in three channel models: the Gaussian channel, the Rayleigh, slow, flat fading channel and the Rayleigh, slow, frequency-selective fading channel. Each of these channels is described in detail below.

2.1 Gaussian channel

The most common channel model encountered in communications systems is the additive white Gaussian noise (AWGN) channel. In this channel, zero-mean white Gaussian noise is added to the transmitted signal s(t), so that the received signal $r(t)$ can be represented as

$$r(t) = s(t) + n(t) \tag{2.1}$$

where $n(t)$ is a zero-mean white Gaussian noise process. $\frac{N_o}{2}$ is the power spectral density of the noise term $n(t)$.

2.2 Small Scale Fading Channels

Small scale fading occurs due to multipath components in a channel. Small scale fading consists of two independent mechanisms: the time spreading of the signal and the time varying behavior of the channel. The time varying behavior of the channel causes a Doppler shift. The Doppler shift is a measure of the spectral broadening of the signal caused by the relative motion of the receiver with respect to the transmitter. The Doppler shift f_d is a function of the speed of the receiver. In our WM experiments, we employed the following two Doppler shifts.

1. Military communications: For military communications, frequency allocations are in the 900MHz range. Assuming a vehicle speed of $45mph$, the Doppler shift is $f_d = 60$Hz.

2. Cellular communications: For GSM 1800, spectrum allocations are in the range of 1800MHz. IMT 2000 specifications for spectrum allocations are in the range of 1900MHz. Taking a carrier frequency of $f_c = 1800$MHz, and vehicle speeds of $45mph$, the Doppler shift is $f_d = 120$Hz.

This Doppler shift impacts whether the channel can be described as slow fading or fast fading. In a fast fading channel, the coherence time, T_C, of the channel is smaller than the symbol duration of the transmitted signal (i.e. $T_S > T_C$). In a slow fading channel, the channel impulse response changes at a rate much slower than the transmitted baseband signal, $s(t)$ and the symbol period of the signal is much smaller than the coherence time of the channel $T_S << T_C$ [12]. In our WM trials, the longest symbol period occurs at the lowest scale (scale 10), $T_S = 0.977$ms. This value is much smaller than the coherence time given by $T_C = \frac{0.423}{f_d} = 7.05$ms for $f_d = 60$Hz and $T_C = 3.5$ms for $f_d = 120$Hz. Hence, the small scale fading channel models considered in Sections (2.2.1) and (2.2.2) are slow fading channels.

2.2.1 Flat Fading Channel

The time dispersion in a multipath environment causes the signal to undergo either flat or frequency selective fading. If the channel has a constant gain and linear phase response over a bandwidth that is greater than the bandwidth of the transmitted signal, then the received signal undergoes flat fading (i.e. the received signal is not distorted by intersymbol interference). In a flat fading channel the signal bandwidth is much smaller than the coherence bandwidth of the channel (i.e. $B_S << B_C$). Alternatively, time dispersion can be described in terms of the symbol period, T_S. In a flat fading channel T_S is much larger than the root-mean-square (rms) delay spread of the channel, σ_τ. In our WM trials T_S at scale 10 is 0.977ms and T_S at scale 13 is 122μs. The form of our simulated model, equation (2.2), results in a flat fading channel for all scales (i.e. $\sigma_\tau << T_{S13} < T_{S10}$) since σ_τ is effectively zero in this model.

Small scale fading can be modeled as a Rayleigh distribution [12, 14]. The received signal is given by

$$r(t) = s(t)ray(t) + n(t) \tag{2.2}$$

As in the AWGN channel, $s(t)$ is the transmitted signal and $n(t)$ represents thermal and device noise (it also still dictates the SNR). The impact of the Rayleigh, flat, slow fading channel is given by the multiplicative $ray(t)$ [12]. $r(t)$ is coherently demodulated; perfect carrier synchronization is assumed at the receiver.

2.2.2 Frequency Selective Fading Channel

If the bandwidth of the signal of interest exceeds the coherence bandwidth of the channel, the signal undergoes frequency selective fading (i.e. $B_S > B_C$). Viewed in the frequency domain, the channel causes different levels of attenuation for different frequency components of the signal. Frequency selective fading is caused by multipath delays which approach or

exceed the symbol period of the transmitted symbol (i.e. $T_S < \sigma_\tau$), where σ_τ is still the rms delay spread of the channel. In practice, $T_S \leq 10\sigma_\tau$ will result in a frequency selective channel; the channel introduces ISI.

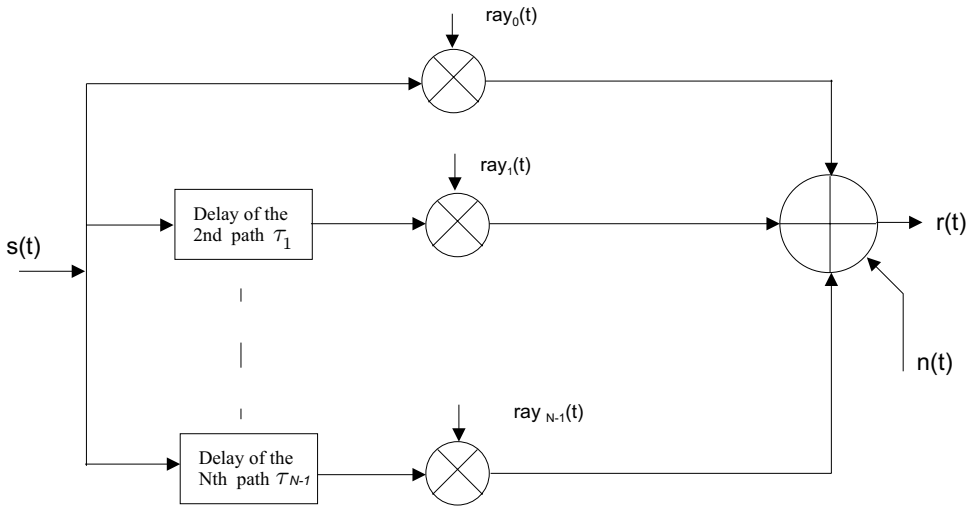

Figure 2.1: Frequency-selective channel model.

We used a two-ray channel model with a variable rms delay spread σ_τ. (σ_τ was varied between 0.2μs and 120μs). In propagation measurements by T.S. Rappaport, et. al. [15] at 900MHz, urban areas typically had rms delays in the range of $2-3\mu s$, hilly residential areas had rms delays in the range of $5-7\mu s$ and worst case rms delay spreads were of the order of $20\mu s$. Excess delays in the range of $100\mu s$ were also observed. For the frequency selective fading channel, the received signal is given by

$$r(t) = \alpha_0 ray_0(t)s(t) + \alpha_1 ray_1(t)s(t-\tau_1) + n(t) \tag{2.3}$$

where α_0 and α_1 are the amplitudes of the main ray and the secondary ray respectively. The signal energy in the main component along with the power of the noise term, $n(t)$, determines the SNR of the signal. The secondary component with a factor of α_1 and delayed by τ_1 corresponds to the first multipath bin with significant amplitude.

The rms delay spread is defined as [12]

$$\sigma_\tau = \sqrt{\overline{\tau^2} - (\overline{\tau})^2} \tag{2.4}$$

where $\overline{\tau}$ is the mean excess delay and is defined by

$$\overline{\tau} = \frac{\sum_k P(\tau_k)\tau_k}{\sum_k P(\tau_k)} \tag{2.5}$$

where $P(\tau_k)$ is the power of the kth component (ray) and is obtained from the power delay profile of the channel and τ_k is the delay of the kth component. All delays are measured relative to the first signal arriving at $\tau_0 = 0$. The second moment of the power delay profile ($\overline{\tau^2}$) is given by

$$\overline{\tau^2} = \frac{\sum_k P(\tau_k)\tau_k^2}{\sum_k P(\tau_k)}. \tag{2.6}$$

For our experiments we simulate two paths so that $k = 0$ and $k = 1$. Furthermore, in many of our trials, $\alpha_0 = \alpha_1$; thus equation (2.4) simplifies to $\sigma_\tau = \frac{\tau}{2}$. $P(\tau_k)$ is given by α_k^2 where α_k is the amplitude(gain) of the kth ray.

The sum of $E\{\alpha_0^2 ray_0(t)^2\}$ and $E\{\alpha_1^2 ray_1(t)^2\}$ is set to unity so that the channel has an average power gain of one [16]. This is to ensure that the average signal energy at the input and output of the channel remains the same. A generalized block diagram of a frequency selective channel is shown in Figure 2.1 for an N-path channel. For our frequency-selective channel in (2.3), N=2 [12].

In Figure 2.1, the Rayleigh waveform $ray_{N-1}(t)$ can be generated using Clarke and Gans's fading model [1, 6]. A Rayleigh fading waveform can be simulated by generating independent inphase and quadrature complex Gaussian noise samples and filtering them by $H(f)$ as shown in Figure 2.2. $S_{E_z}(f)$ is the spectrum of the Doppler filter. Particularly, it has been shown that for an omni-directional $\lambda/4$ antenna with a gain of 1.5, the Doppler spectrum is given by

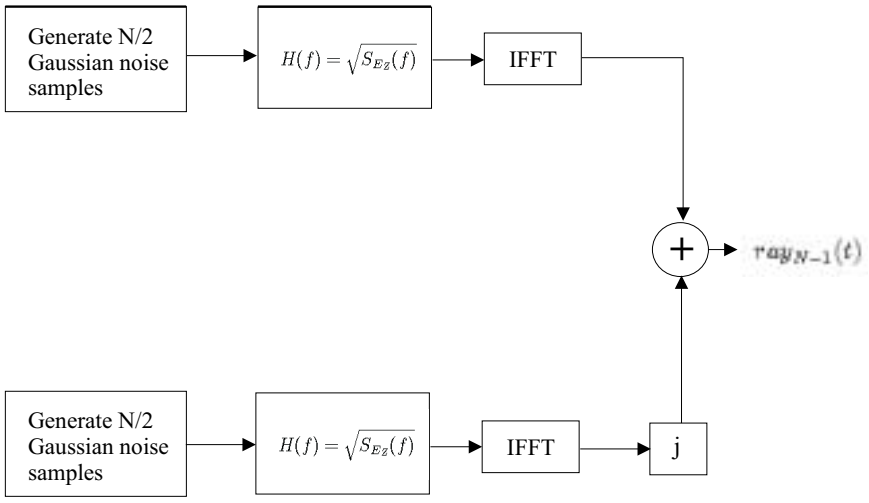

Figure 2.2: Generation of a Rayleigh fading waveform [16].

$$S_{E_z}(f) = \frac{1.5}{\pi f_m \sqrt{1 - (\frac{f - f_c}{f_m})^2}} \tag{2.7}$$

where f_c is the center frequency and f_m is the maximum Doppler spread. f_c is zero and f_m takes values of 60Hz and 120Hz. The sum of the inphase and quadrature terms at the output of the IFFT forms the complex Rayleigh fading waveform $ray_{N-1}(t)$. The waveform has a Rayleigh distributed amplitude and a uniformly distributed phase in the interval $[0, 2\pi)$. The rms value of the envelope is normalized to one. This normalization ensures that the average signal energy is not altered when passed through the channel simulator. This complex, normalized waveform is denoted as $ray_{N-1}(t)$ in Figure 2.2. These Rayleigh waveform generators are used to generate each of the $ray_k(t)$ in Figure 2.1 where k is from 0 to N-1. The waveform $ray(t)$ in equation (2.2) is obtained by taking only the envelope component (i.e. $ray(t) = |ray_{N-1}(t)|$) of the complex fading waveform generated in Figure 2.2.

Chapter 3

Wavelet Modulation

3.1 Multiresolution Analysis

Wavelet analysis involves decomposition of the signal of interest, $s(t)$, into subspaces on $L^2(R)$; the signal is projected onto these nested subspaces, V_m. The subspace, V_m, is contained in the next finer subspace V_{m+1}. This is represented as

$$... \subset V_m \subset V_{m+1} \subset V_{m+2} \subset ... \tag{3.1}$$

Equation (3.1) implies that a function in one subspace is also present in all finer subspaces.

In general, V_m has a basis of $\{2^{m/2}\phi(2^m t - n); n \in \mathcal{Z}\}$ where $\phi(t)$ is the scaling function. $\phi(t)$ is orthogonal to its translations $\{\phi(t-n); n \in \mathcal{Z}\}$; however, $\phi(t)$ is not orthogonal across dilations $\{\phi(2^m t); m \in \mathcal{Z}\}$.

The wavelet space W_m is defined as the difference between V_m and V_{m+1}. It is the orthogonal

complement of V_m in V_{m+1} and can be represented as

$$V_{m+1} = V_m \oplus W_m \tag{3.2}$$

The subspace W_m contains the detail information of the signal $s(t)$, whereas V_m contains the average or approximate information of the signal. If $s_m(t)$ is the projection of $s(t)$ onto the subspace V_m, and $s_{m+1}(t)$ is the projection of $s(t)$ onto the subspace V_{m+1}, then the information $\Delta s_m(t) = s_{m+1}(t) - s_m(t)$ is the detail information contained in W_m. There exists a wavelet function $\psi(t)$ such that all of its translations at scale m, $\{2^{m/2}\psi(2^m t - n); n \in \mathcal{Z}\}$ forms an orthonormal basis for the subspace W_m. The relationship between the V_m and W_m subspaces is shown in Figure 3.1.

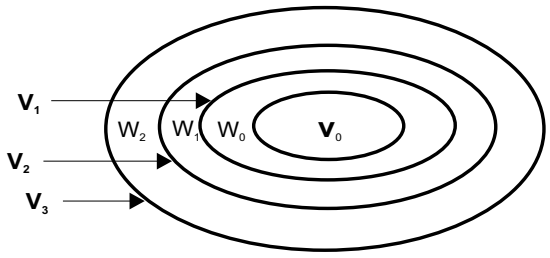

Figure 3.1: Multiresolution analysis showing the relationship between the V_m and W_m subspaces.

$\psi(t)$ is orthogonal (in the sense of the usual L^2 inner product) to its scalings $\psi(2^m t)$ (dilations for $m < 0$; compressions for $m > 0$) and to the translations $\psi(2^m t - n)$ of its scalings. The set of all scalings and translations $\{\psi_n^m(t) = 2^{m/2}\psi(2^m t - n); m, n \in \mathcal{Z}\}$ forms a complete orthonormal basis for $L^2(R)$.

Two wavelets are employed in the simulations: the Daubechies $N = 4$ wavelet and the Daubechies $N = 8$ wavelet. Both are orthogonal, compactly supported wavelets. Figure 3.2 depicts the wavelet and scaling functions for the Daubechies $N = 4$ wavelet. As seen in Figure 3.2, the $N = 4$ wavelet has a support size of 7 and 4 vanishing moments. The Daubechies $N = 8$ wavelet has a support size of 15 and 8 vanishing moments.

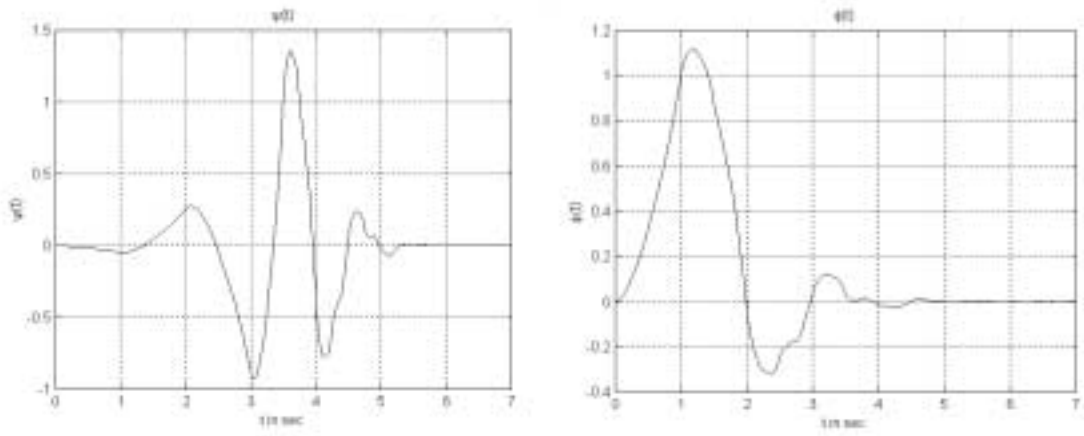

Figure 3.2: The Daubechies $N = 4$ wavelet function $\psi\ (t)$, and scaling function $\phi(t)$.

3.2 Discrete Wavelet Transform

Wavelets are waveforms with the desirable characteristic of localization in both time and frequency. They also possess the property of orthogonality across scale and translation [4].

The wavelet representation of a signal $s(t)$ is given by

$$s_n^m = \int_{-\infty}^{\infty} s(t) 2^{m/2} \psi(2^m t - n)\, dt \tag{3.3}$$

$$s(t) = \sum_{m=-\infty}^{\infty} \sum_{n=-\infty}^{\infty} s_n^m 2^{m/2} \psi(2^m t - n) \tag{3.4}$$

where $\psi(t)$ is the wavelet function [4].

Equation (3.3) is the discrete wavelet transform (DWT) and (3.4) is the inverse discrete wavelet transform (IDWT). Mallat's fast wavelet transform (FWT) provides a computationally efficient, practical, discrete time algorithm for computing the DWT [7]. A multiresolution analysis approach is used to explain Mallat's FWT. Let A_{m+1} be the projection operator which approximates the signal at resolution 2^{m+1}. $\phi_n^{m+1} = \{2^{m+1}\phi(2^{m+1}t - n); n \in Z\}$ is an orthonormal basis for V_{m+1}. The resolution limited approximation of a signal $s(t)$ is given

by

$$A_{m+1}s(t) = \sum_n a_n^{m+1}\phi_n^{m+1}(t) \tag{3.5}$$

where a_n^{m+1} are the approximation coefficients obtained by the projection of $s(t)$ onto the basis functions

$$a_n^{m+1} = \int_{-\infty}^{\infty} s(t)\phi_n^{m+1}(t)dt. \tag{3.6}$$

The approximation and wavelet coefficients at any coarser scale can be calculated by

$$a_n^m = \sum_l h(l-2n)a_l^{m+1} \tag{3.7}$$

$$s_n^m = \sum_l g(l-2n)a_l^{m+1} \tag{3.8}$$

where $h(-n)$ and $g(-n)$ are the lowpass and highpass filters in the asssociated 2 channel analysis filter bank. Equations (3.7) and (3.8) represent the FWT to compute the DWT in equation (3.3). Figure 3.3 shows the analysis filter bank corresponding to the DWT.

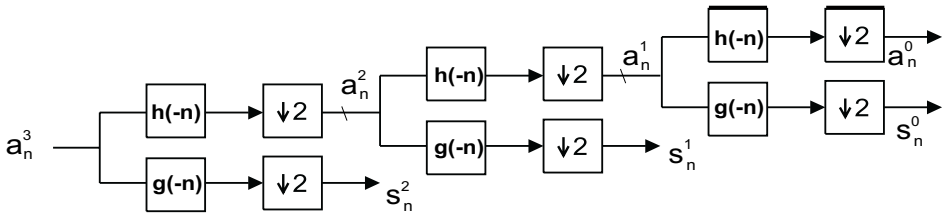

Figure 3.3: A 2 channel analysis filter bank used to compute the DWT.

Conversely, it is possible to reconstruct the approximation coefficients a_n^m using

$$a_n^{m+1} = \sum_l h(2l-n)a_l^m + g(2l-n)s_l^m. \tag{3.9}$$

The reconstruction (synthesis) operation is shown in Figure 3.4. This is the IFWT for computing the IDWT in equation (3.4). In the Figure 3.4, $h(n)$ and $g(n)$ are the lowpass

and highpass synthesis filters. The lowpass filter, $h(n)$, satisfies the following orthogonality condition

$$\sum_n h(n)h(n-2k) = \delta(k). \tag{3.10}$$

The highpass filter is obtained from the lowpass filter by

$$g(n) = (-1)^n h(N-n) \tag{3.11}$$

where $(N+1)$ is the filter length.

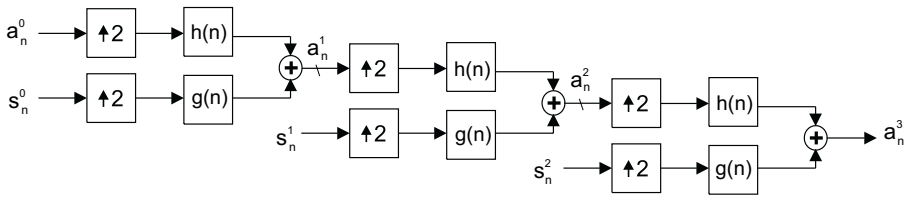

Figure 3.4: A 2 channel synthesis filter bank to compute the IDWT.

Together, equations (3.7), (3.8) and (3.9) form the DWT and the IDWT. These discrete time algorithms with filter bank implementations are used in WM.

3.3 Wavelet Modulation Basics

The wavelet modulated signal to be transmitted, $s(t)$, can be generated via

$$s(t) = \sum_{m=-\infty}^{\infty} \sum_{n=-\infty}^{\infty} \beta^{-m/2} x[n] 2^{m/2} \psi(2^m t - n) \tag{3.12}$$

where $x[n]$ is the data that is modulated onto the wavelet at different scales. $\beta = 2^{2H+1}$ where H refers to the degree of the homogeneous signal. A homogeneous signal $y(t)$ satisfies the deterministic self-invariance property

$$y(t) = a^{-H} y(at) \tag{3.13}$$

where H is the degree of the homogeneous signal and $a > 0$ [19]. We take $H = -\frac{1}{2}$ so that $\beta = 1$ in equation (3.12). Notice that $s(t)$ is completely specified by $x[n]$ and vice versa; $x[n]$ is referred to as the generating sequence for the transmitted signal $s(t)$.

In a practical system $x[n]$ is modulated onto a finite number of contiguous, octave-width frequency bands (i.e. m has finite limits—there are a finite number of scales available). Consequently, the transmitted signal $s(t)$ is given by

$$s(t) = \sum_{n=-\infty}^{\infty} \sum_{m \in M} \beta^{-m/2} x[n] 2^{m/2} \psi(2^m t - n) \tag{3.14}$$

where M is a finite set of contiguous integers.

For the data to be recovered at rate 2^m, the smallest baseband bandwidth that can be used is 2^{m+1}Hz. This results in a bandwidth efficiency of $\eta_F = 0.5$bits/sec/Hz. This represents a disadvantage of WM when compared to traditional modulation schemes like QPSK or 16-QAM with bandwidth efficiencies of $\eta_F = 2.0$bits/sec/Hz and $\eta_F = 4.0$bits/sec/Hz (assuming optimal pulse shaping), respectively.

However, WM has an advantage over traditional modulation schemes in its novel multirate diversity. For instance, WM works well in fading environments where other modulation techniques suffer poor performance: in WM, if some frequency bands are corrupted, then the message can still reach the receiver on one of the uncorrupted frequency bands (i.e. scales). In other words, only one copy of the message needs to get through. This advantage has not been explored in the previous research. We present simulation results indicating WM's advantage in Chapter 5.

3.4 Wavelet Modulation Implementation

Our simulations have been carried out for two different sets of scales. Therefore, the scale parameter m takes on two sets of values:

1. $m \in M$ where $M = \{10, 11, 12, 13\}$; this corresponds to a data rate of $R_b = 1024$bps for binary data at the coarsest scale ($m = 10$) and $R_b = 8192$bps at the finest scale ($m = 13$). For demodulation at the receiver, a baseband bandwidth of 2^{m+1}Hz is required [19]. Consequently, demodulation at scale $m = 13$ requires a bandwidth of $2^{13+1} = 16$kHz.

2. $m \in M$ where $M = \{14, 15, 16, 17\}$; this corresponds to a data rate of $R_b = 16.384$kbps for binary data at the coarsest scale ($m = 14$) and $R_b = 131$kbps at the finest scale ($m = 17$).

The data to be transmitted takes on one of two equally likely values

$$x[n] \in \{+\sqrt{E_b}, -\sqrt{E_b}\} \tag{3.15}$$

where E_b is the energy per bit.

By comparing equations (3.4) and (3.12) and recalling that $\beta = 1$, we notice that the wavelet coefficients of $s(t)$ correspond to the data $x[n]$. Thus, $x[n]$ is used in place of s_l^m in equation (3.9) to obtain the approximation of $s(t)$ at scale $m + 1$. Notice that to compute the transmitted signal $s(t)$ we use the IFWT (3.9) in place of equation (3.14); a_n^{m+1} is the approximation of $s(t)$ at scale $m + 1$.

The data to be transmitted, $x[n]$, is split into blocks of length $L = 1024$. To begin the generation of $s(t)$, we begin at the coarsest scale $m = 10$; the data is convolved with the filter coefficients of the high pass filter, $g(n)$. Equation (3.9) simplifies to

$$a_n^{11} = \sum_l g(2l - n) x_l^{10} \tag{3.16}$$

where x_l^{10}, the data to be transmitted at scale 10, is given by the vector $x_l^{10} = x = [x[0], x[1], \ldots x[1023]]$.

Twice the amount of data is required to modulate the data onto the next higher scale. A periodic replication of the data results in $x_l^{11} = [x\ x] = [x[0], x[1], \ldots x[1023], x[0], x[1], \ldots x[1023]]$. Then a_n^{12}—the approximation of $s(t)$ at scale 12—is obtained via (3.9)

$$a_n^{12} = \sum_l h(2l-n)a_l^{11} + g(2l-n)x_l^{11}. \tag{3.17}$$

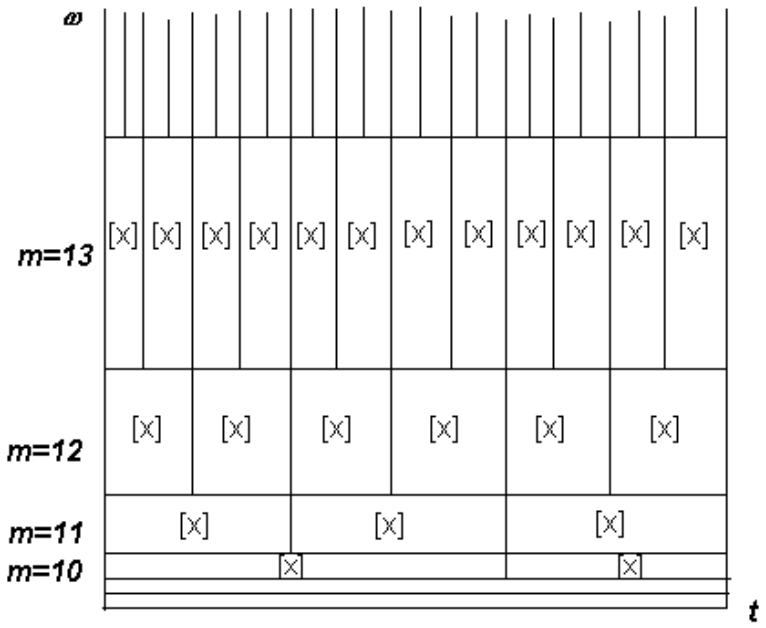

Figure 3.5: Time-frequency portrait of the transmitted signal $s(t)$. $[x]$ represents data blocks of length $L = 1024$ bits.

A view of the transmitted signal in the time-frequency plane is shown in Figure 3.5. At scale 11 there is twice the amount of data at scale 10. Equation (3.17) is repeated until the coefficients at scale 14, a_n^{14}, are obtained. These coefficients are iterated through the filter bank again with $x_l^m = 0$ until approximation coefficients at scale 17, a_n^{17}, are obtained; this

results in a close approximation to the signal $s(t)$ with a sampling rate of 131072 samples/sec. This signal is then transmitted over the channel to the receiver.

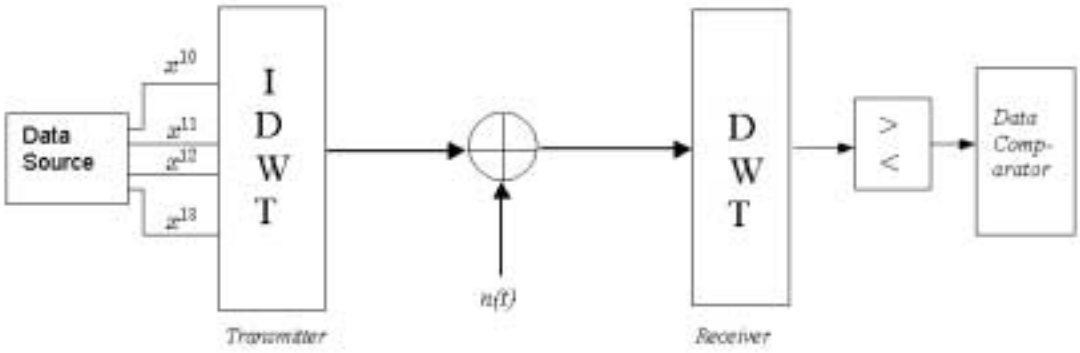

Figure 3.6: Block diagram of WM simulator with an additive white Gaussian noise channel.

Figure 3.6 depicts a block diagram overview of the WM simulator implementation. The IDWT (implemented using the IFWT) performs the function of the transmitter and the DWT (implemented using the FWT) performs the function of the receiver. The decision device estimates the transmitted bit from the received data. If the received data is greater than zero, then the transmitted bit is $+\sqrt{E_b}$; if not, then the transmitted bit is $-\sqrt{E_b}$. The data comparator/verification step compares the received data with the transmitted data and determines the error rate. An error occurs if the received bit does not match the transmitted bit. This representation of WM is a near baseband type of implementation. In practice, the output signal $s(t)$ would be multiplied by a carrier at some passband frequency, ω_c, to obtain the bandpass signal.

Figure 3.7 shows the spectral characteristics of the WM signal $s(t)$. The spectrum has been plotted against normalized frequency f. The mainlobe width corresponds to $f \approx 0.1$. The WM signal is observed to have a null in the spectrum at DC; this is expected, since wavelets are bandpass signals and have no DC component. The first sidelobe is 25dB below the main lobe. On passing this signal through a filter to obtain only the main lobe, little variation in the performance of WM results [10].

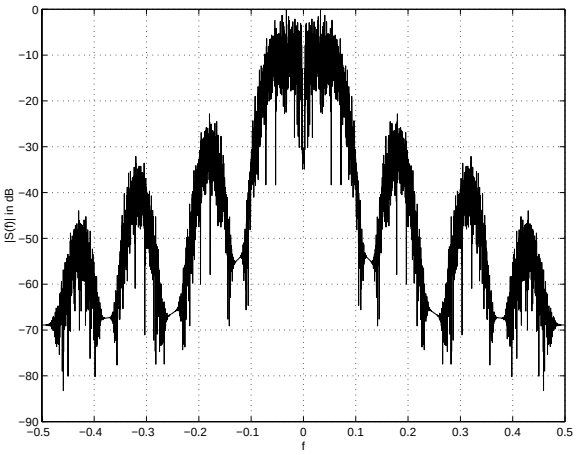

Figure 3.7: Spectrum of WM signal, $S(f)$. The mainlobe has a bandwidth of $f = 0.1$ where f is the normalized frequency.

3.5 Previous Research on Wavelet Modulation

Wornell and Oppenheim outlined the receiver design and performance of WM for an additive, white, Gaussian noise (AWGN) channel [18, 19]. The transmitted message was a random, finite length L, binary-valued sequence(i.e. $x[n] \in \{+\sqrt{E_b}, -\sqrt{E_b}\}$). First the receiver extracts the wavelet coefficients $R(i, j)$ from the received signal $r(t)$ via the DWT (3.3). The duration-bandwidth characteristics of the channel affect which wavelet coefficients, $x(m, n)$, are computed as well as how many noisy observations K of each of the L samples in $x[n]$ are available. The performance was shown to be given by

$$P_e = \mathrm{Q}(\sqrt{K\sigma_c^2}) \tag{3.18}$$

where σ_c^2 is the SNR in the channel. Equation (3.18) satisfies our expectations that the probability of error decreases as the number of observations increases and as the SNR increases.

Zarowski presented a useful follow-up to Wornell and Oppenheim's research [21]. This practical work outlined two structures for implementing the modulated signals described in the earlier work.

Ptasinski and Fellman implemented a WM system using the Daubechies $N = 4$ wavelet [4] and evaluated its performance in an AWGN channel [10]. They replicated Wornell and Oppenheim's results that showed that one-scale demodulation gave BER performances almost identical to binary phase shift keying (BPSK). Furthermore, a linear phase, lowpass, finite impulse response (FIR) was employed to filter the transmitted signal, $s(t)$. These trials indicated that BER was not significantly impacted; however, the bandwidth efficiency of the main lobe after filtering approached the theoretical 0.5bits/sec/Hz. Ptasinski and Fellman also derived the theoretical bit-error performance of WM and showed that it was equivalent to BPSK (i.e. $P_e = \mathrm{Q}(\sqrt{\frac{2E_b}{N_o}})$) where E_b is the energy per bit and $\frac{N_0}{2}$ is the variance of the noise and SNR is given by $\frac{E_b}{N_0/2}$ [11]. This is equivalent to equation (3.18) for $K = 1$.

It is useful to note that in all of the previous research results for WM, only one scale was used in the demodulation of the received signal. The redundancy in the received signal—within and across different scales–was not exploited to improve BER performance. Also, previous research results have not explored the performance of WM in flat and frequency-selective channels.

Chapter 4

New Methods to Exploit Multirate Diversity

4.1 Joint Estimation Strategies

Figure 3.5 shows the time-frequency diagram for the transmitted signal $s(t)$. This figure illustrates the data replication with respect to the scales: the higher the frequency band, the larger the amount of data. This redundancy in the transmitted signal occurs over time and also over frequency and can be used to the advantage of the receiver. The receiver can utilize any one of the copies of data at any of the frequency bands for demodulation. This choice is dictated by the time-bandwidth limitations of the channel.

More importantly, this data redundancy can be used to improve the bit error rate performance of the receiver by utilizing more than one noisy observation of the data at one or more scales. For example, consider the data modulated onto scale 10; it is given by

$x_n^{10} = x = [x[0], x[1], \ldots x[L-1]]$, where L is the length of the finite data vector. The data modulated onto scale 11 is twice this length (i.e. $2L$). where $x_n^{11} = [x\ x] = [x[0], x[1], \ldots x[L-1], x[0], x[1], \ldots x[L-1]]$. At the receiver, the data has been corrupted by a noisy channel. When the estimate of a received bit is obtained using more than one noisy observation, it is possible to calculate an improved estimate. Since the estimate is determined using 2 or more noisy observations, the strategy is termed joint estimation and the statistic obtained is called a joint statistic.

Joint estimation at the receiver is accomplished by averaging the noisy observations. Let $\hat{x}[0]$ be the joint statistic of $x[0]$; also let $\tilde{x}^{10}[0]$, $\tilde{x}_1^{11}[0]$ and $\tilde{x}_2^{11}[0]$ be the noisy observations of $x[0]$ at scales 10 and 11. The estimate of $x[0]$ is calculated as

$$\hat{x}[0] = \frac{\tilde{x}^{10}[0] + \tilde{x}_1^{11}[0] + \tilde{x}_2^{11}[0]}{3}. \tag{4.1}$$

Define K as the redundancy factor (i.e. number of observations used to arrive at an estimate). In equation (4.1), $K = 3$. In general, as K increases, the accuracy of the joint statistic improves.

We would expect this joint estimation strategy to improve BER performance in an AWGN channel, and in a Rayleigh flat fading channel, since the data is equally corrupted at all scales. However, this would not be true in a frequency-selective channel. If noisy observations are used from some severely distorted frequency band along with noisy observations from a less corrupted frequency band, then the BER performance would be lower than that derived from just the noisy observations at the less corrupted band. Our simulation results verify these expectations. The results of this joint estimation strategy for all 3 channels are described in Chapter 5, Section 5.6.

4.2 Channel Identification and ISI Detection

The analysis of the noisy, wavelet modulated signal at the receiver allows two things to occur: channel identification and ISI detection and removal. This situation is unique to WM due to the redundancy offered by the WM signal across time and frequency. A decision on which copies of data to use for demodulation, along with the number of copies to use, depends on the channel type. Channel identification is accomplished at the receiver using a statistical approach. If the channel is identified as an AWGN or a flat fading channel, then a joint statistic using all available data copies gives the best estimate of the transmitted data. If the channel is frequency-selective in nature, then an estimate of the channel rms delay spread is generated. This dictates which data copies are used to yield the best estimate of the transmitted data.

4.2.1 Channel Identification

Figure 4.1 illustrates the variation of mean values across scale for the three channels used in the simulation (i.e. AWGN channel, Rayleigh flat fading channel at 60Hz, and the frequency-selective fading channel at 60Hz). The chart shows the mean of those data bits greater than zero after demodulation, but before the decision device. For the AWGN and flat fading channels, the means do not differ appreciably across the scales. However, Figure 4.1 shows large variations in the means across scale for the frequency-selective channels. For the frequency-selective channel, the distortion caused by ISI depends primarily on the rms delay spread σ_τ of the channel. When σ_τ is of the order of the bit period of scale 13 ($\sigma_\tau = \frac{T_{s_{13}}}{4}$), the mean values increase for decreasing scale. Hence, scale 10 is observed to have the highest mean and scale 13, the lowest mean. When σ_τ is of the order of scale 15 ($\tau = \frac{T_{s_{15}}}{4}$), scale 15 has the lowest mean value and mean values increase from scale 15 to scale 14. The scale at which the rms delay spread, σ_τ is of the order of the bit period has the lowest mean among

all the scales. This gives an indication of the rms delay spread value. This information is used to determine which scales can be used for demodulation, as explained in Section 4.2.2.

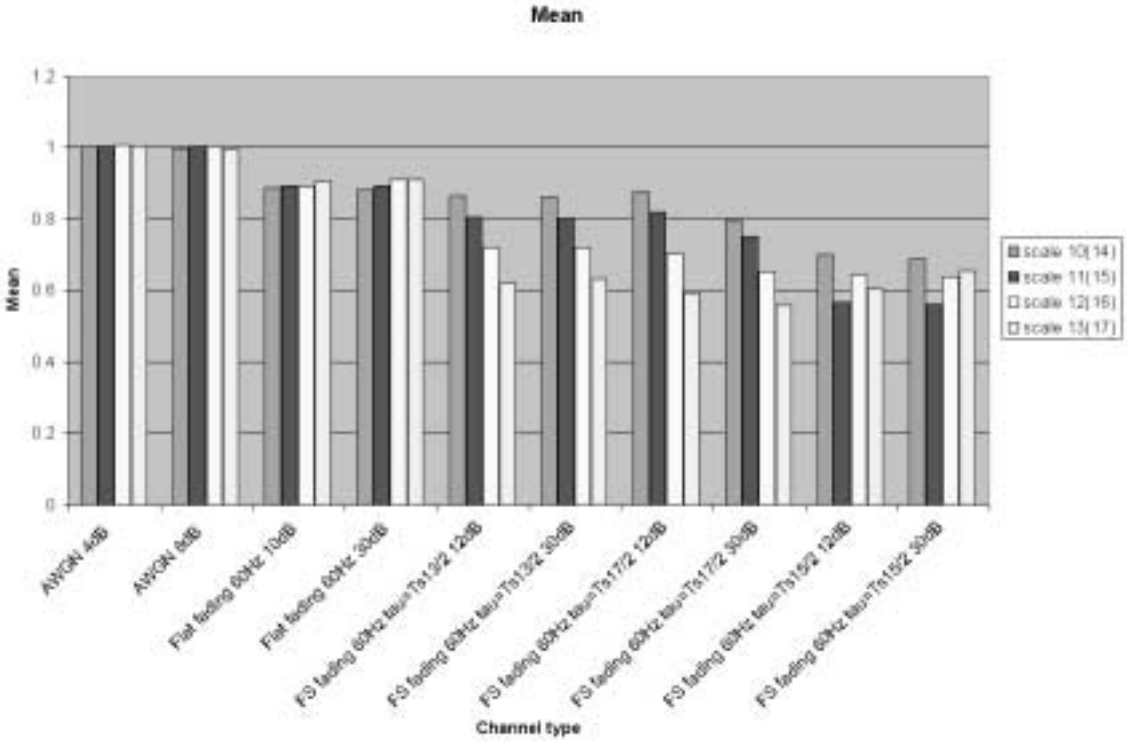

Figure 4.1: Chart showing mean values of data in different channels (These mean values are calculated using only the received bits greater than zero). For the frequency-selective channel, $\alpha_0 = 0.707$ and $\alpha_1 = 0.707$. Each mean value is obtained using $N = 10$ trials of 1000 data bits each.

A statistical one-way analysis of variance (ANOVA) scheme is used to classify the channel type. Here, the null hypothesis (H_0) posits that the means across scale are equal. The alternative hypothesis (H_1) posits that the means across scale are not equal.

The received data bits that are greater than zero for all scales form the set of observations. Each scale is referred to as a treatment. For our analysis there are 4 treatments—one for

each of the scales. The ANOVA scheme takes the set of observations and determines the mean value for each of the treatments (scales) and generates an F statistic.

The F statistic is defined as [5]

$$F = \frac{\frac{SSTr}{(I-1)}}{\frac{SSE}{I(J-1)}} \tag{4.2}$$

where: SSE (error sum of squares) measures the data variation that is unexplained by any difference or similarities in the means across scale; SSTr (treatment sum of squares) measures the data variation that is explained by differences in the means across scales; I is the number of treatments (for our analysis, $I = 4$ scales); and J is the number of observations in each treatment (for our analysis, $J = 1000$ demodulated bits).

Notice that when the explained variation is large compared to the unexplained variation, F is also large and the null hypothesis, H_0, is rejected in favor of the alternative hypothesis, H_1 (i.e. the means across scale are not equal). In particular, for a significance level $\alpha = 0.05$ test, $F \geq 2.6$ would result in a rejection of H_0. Similarly, for a significance level $\alpha = 0.01$ test, $F \geq 3.78$ would result in a rejection of H_0. A significance level α test indicates the probability of a type I error (α): the null hypothesis H_0 is rejected when H_0 is in fact true.

Table 4.1: ANOVA statistics for AWGN channel

E_b/N_0	SSE	SSTr	F
4dB	301.9	0.0345	0.1459
8dB	304	0.1794	0.7548

Table 4.1 shows the F-statistic, SSE and SSTr values for two trials with the AWGN channel. Both F values are small enough so that H_0 is accepted at either significance level. The large

SSE values and small SSTr values indicate that the data variation is not due primarily to differences in the means across scale.

Table 4.2: ANOVA statistics for the three channel types

Channel	E_b/N_0	σ_τ	F
AWGN	4dB	—	0.30
AWGN	8dB	—	0.65
Flat Fading	10dB	—	2.85
Flat Fading	30dB	—	2.72
Frequency-Selective Fading	12dB	$0.25T_{S_{17}}$	60.51
Frequency-Selective Fading	30dB	$0.25T_{S_{17}}$	49.46
Frequency-Selective Fading	12dB	$0.25T_{S_{15}}$	49.22
Frequency-Selective Fading	30dB	$0.25T_{S_{15}}$	39.10

Next consider an analysis of all three channel types. Table 4.2 shows the average value of the F statistic obtained for 20 trials of 1000 data points each. These trials examined the AWGN, the flat fading and the frequency-selective fading channels (at $f_d = 60$Hz) at two SNR levels. Notice that for the AWGN channel, the computed F values always resulted in an acceptance of H_0 ($F < 2.6$ in all cases). For the frequency-selective fading channel, the computed F values always resulted in a rejection of H_0 at the $\alpha = 0.01$ level ($F \geq 3.78$ in all cases). Therefore, the F statistic differentiates the AWGN and the frequency-selective fading channels.

For the flat fading channel, the computed F values ranged from 1.5 to 13 with an average value of 2.78. Thus, after the initial ANOVA was performed (and H_0 was either accepted or rejected), a subsequent test was conducted. To differentiate the AWGN channel and the flat

fading channel, a threshold of $F_1 = 1.5$ was used. If H_0 was accepted and $F < 1.5$, then the channel was classified AWGN, otherwise it was classified as flat fading. To differentiate the frequency-selective channel and the flat fading channel, a threshold of $F_2 = 13$ was used. If H_0 was rejected and $F > 13$, then the channel was classified frequency-selective. Otherwise it was classified as flat fading.

Now consider two other frequency-selective fading channel cases: all scales are corrupted by ISI ($\sigma_\tau > \frac{T_{S_{min}}}{4}$ where $T_{S_{min}}$ is the bit period of the lowest scale transmitted) and all scales have little ISI corruption ($\sigma_\tau < \frac{T_{S_{max}}}{4}$ where $T_{S_{max}}$ is the bit period of the highest scale transmitted). When $\sigma_\tau \approx \frac{T_{S_{13}}}{4}$ and the scales being transmitted are 14 through 17, the means across scales are different (Figure 4.2). The mean values for the scales did not show as large a variation as those observed for the frequency-selective channels in Figure 4.1; however, they are lower than those for the flat fading channel. Now the F statistic varied from 4 to 25; thus the F=13 threshold to distinguish flat from frequency-selective would no longer suffice. Instead, a lower F threshold combined with a mean value threshold could separate the two channel types. The detection of ISI is redundant in this case since all the scales (14 through 17) are highly distorted by ISI.

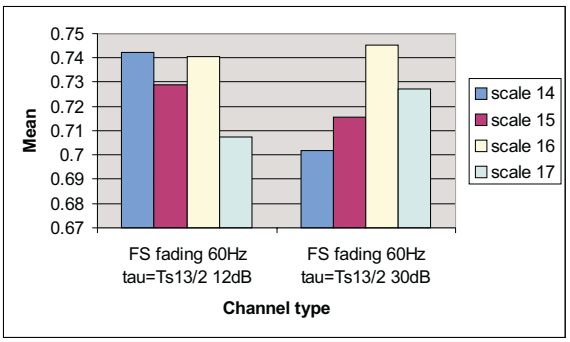

Figure 4.2: Chart showing mean values (by scale) of received data in the frequency-selective channel for $\sigma_\tau = \frac{T_{S_{13}}}{4}$ (These mean values are calculated using only the received bits greater than zero).

Conversely, when $\sigma_\tau \approx \frac{T_{S20}}{4}$ and the transmitted scales are 14 through 17, the channel depicts flat fading characteristics as shown in Figure 4.3. Now the F statistic varied from 2 to 13 (one case had $F > 13$). Since the F values are typically lower than the F=13 threshold, the channel would be correctly identified as flat fading in these cases and ISI detection is unnecessary.

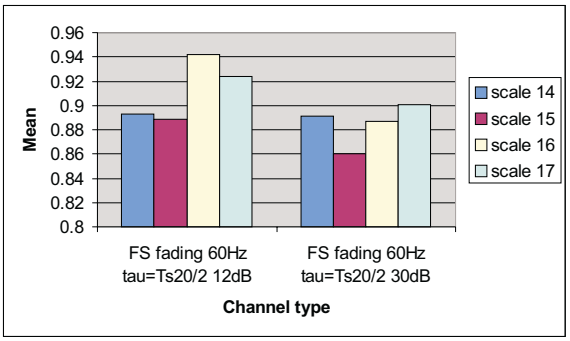

Figure 4.3: Chart showing mean values (by scale) of received data in the frequency-selective channel for $\sigma_\tau = \frac{T_{S20}}{4}$ (These mean values are calculated using only the received bits greater than zero).

4.2.2 ISI Detection

Further processing is required to determine the scale(s) that can be used for demodulation in the frequency-selective channel. In other words, we need to detect which scales are so corrupted by ISI that they cannot be used.

Figure 4.1 illustrates that for the frequency-selective channel, the minimum mean value occurs at the scale where the delay between the main ray and the secondary ray is approximately half the bit period (i.e. $\tau = \frac{T_S}{2}$ or $\sigma_\tau = \frac{T_S}{4}$) (It should be noted that the values of α_0 and α_1 for these simulations are 0.707 and 0.707 respectively).

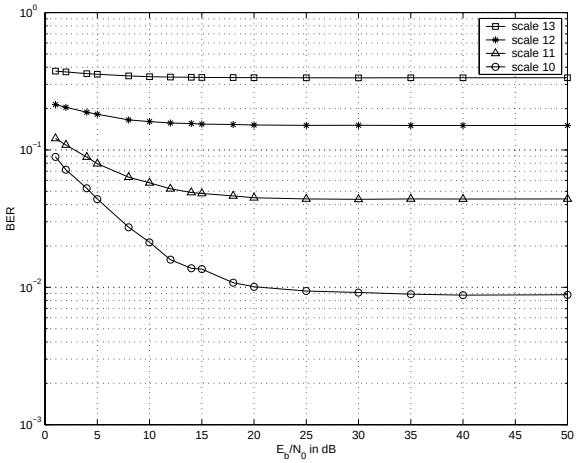

Figure 4.4: Performance of WM in frequency-selective channel at 60Hz, $\sigma_\tau = \frac{T_{s_{13}}}{4}$ (i.e. $\tau = \frac{T_{s_{13}}}{2}$).

Our trials indicate that if the minimum mean value occurs at scale N, then scales N-2 and lower should be used for demodulation. However, the data at scales N-1 and higher are too distorted and should be discarded. For example, if scale 11 corresponds to the minimum mean value, then scales 10 and higher cannot be used for demodulation due to ISI distortion.

Figures 4.4 and 4.5 show the BER curves for $\sigma_\tau = \frac{T_{s_{13}}}{4}$ and $\sigma_\tau = \frac{T_{s_{12}}}{4}$. Notice that when the rms delay spread σ_τ is of the order of the bit period at scale 13, the scales that are least affected by ISI distortion are 10 and 11. When the rms delay is of the order of scale 12 (Figure 4.5), scale 10 shows the best performance; all other scales perform poorly.

This chapter described a joint estimation strategy at the receiver to improve BER performance in the AWGN, flat and frequency-selective fading channels. This chapter also described a new statistical procedure for determinining the channel type and for estimating the rms delay spread in the frequency-selective channel. Experimental results illustrating the effectiveness of our new methods are shown in Chapter 5.

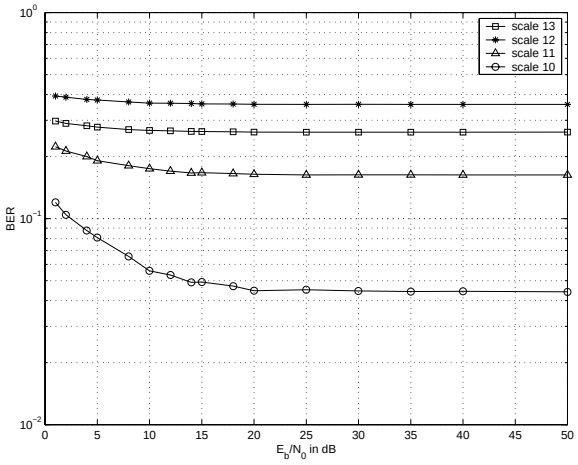

Figure 4.5: Performance of WM in frequency-selective channel at 60Hz, $\sigma_\tau = \frac{T_{s12}}{4}$ (i.e. $\tau = \frac{T_{s12}}{2}$).

Chapter 5

Results

The digital data signal is generated using equation (3.15) with $E_b = 1$. The wavelet modulation (WM) BER performance as a function of SNR is examined for 5 channels: AWGN; Rayleigh flat fading ($f_d = 60$Hz and $f_d = 120$Hz); and, frequency selective fading ($f_d = 60$Hz and $f_d = 120$Hz). Both the flat and frequency selective fading channels are slow fading channels. In Sections 5.1, 5.2, 5.3 and 5.4, demodulation at a particular scale utilizes only 1 copy of the received data at that scale; for the AWGN and flat fading channels, all copies are similar. For the frequency-selective channel we safely assume that all copies of the data at a particular scale are similar. Section 5.6 describes the results obtained using the joint statistic. Section 5.7 illustrates the channel identification and ISI detection and removal algorithm outlined in Chapter 4. All BER results are the average of 8 to 10 independent trials. Both the Daubechies $N = 4$ and $N = 8$ wavelets were used.

5.1 Comparison of $N = 4$ and $N = 8$ Daubechies Wavelets

Figure 5.1 compares the performance of the Daubechies $N = 4$ and $N = 8$ wavelets in a flat fading channel with a Doppler spread of 60Hz. The performance using the $N = 8$ wavelet is shown at scales 10 and 11 and is compared to the $N = 4$ wavelet at scale 10. The $N = 4$ wavelet at scale 10 and the $N = 8$ wavelet at scale 11 have the same compact support (at scale 10, the $N = 8$ wavelet has double the support size of the $N = 4$ wavelet). There is no appreciable performance difference between scales 10 and 11 with the $N = 8$ wavelet; thus, the support size does not seem to be an important factor. For E_b/N_0 values up through 25dB, the two wavelets indicate similar BER performance; however, for $E_b/N_0 \geq 30$dB the $N = 4$ wavelet shows slightly better performance (0.2-0.3dB).

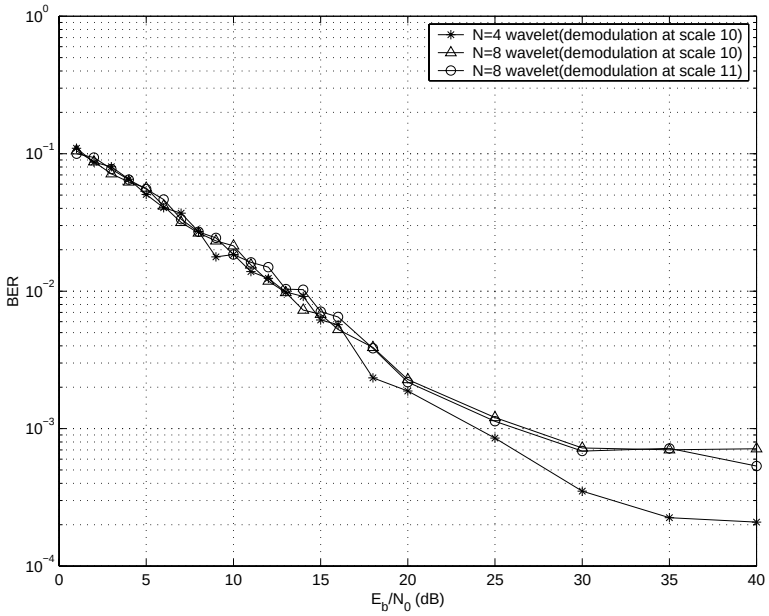

Figure 5.1: Bit Error Rate (BER) vs. E_b/N_0 in a flat fading channel with a Doppler spread of 60Hz. The Daubechies $N = 4$ and $N = 8$ wavelets depict similar performance up through $E_b/N_0 = 25$dB; the $N = 4$ wavelet indicates slightly better performance for higher values of E_b/N_0.

The results obtained using the Daubechies $N = 4$ wavelet did not vary appreciably from the results obtained using the $N = 8$ wavelet for the AWGN and the 120Hz flat fading channels (even for higher values of E_b/N_0). In the remainder of this thesis, all of the results presented for the Daubechies $N = 4$ wavelet also hold for the $N = 8$ wavelet unless explicitly stated otherwise.

5.2 Performance in a Gaussian Channel

Figure 5.2 compares the performance of wavelet modulation with that of theoretical BPSK modulation in an AWGN channel. The BER performance of a BPSK signal in this channel [9] is given by

$$P_e = \mathrm{Q}(\sqrt{\frac{2E_b}{N_0}}). \tag{5.1}$$

This figure indicates that the performance of WM matches BPSK in an AWGN channel (for both the $N = 4$ and $N = 8$ wavelets). The WM performance is depicted for only one scale (scale 10) since performance did not vary across scale. This result verifies Wornell's observations [19] and Ptasinksi's simulated results [10] for WM.

5.3 Performance in Flat Fading Channels

WM performance in the $f_d = 60$Hz and $f_d = 120$Hz flat fading channels, as described in Section 2.2.1, was investigated. Figure 5.3 depicts a linear BER curve inversely proportional to SNR. The curve flattens out at 35dB for demodulation at scales 10 and 11; however, the

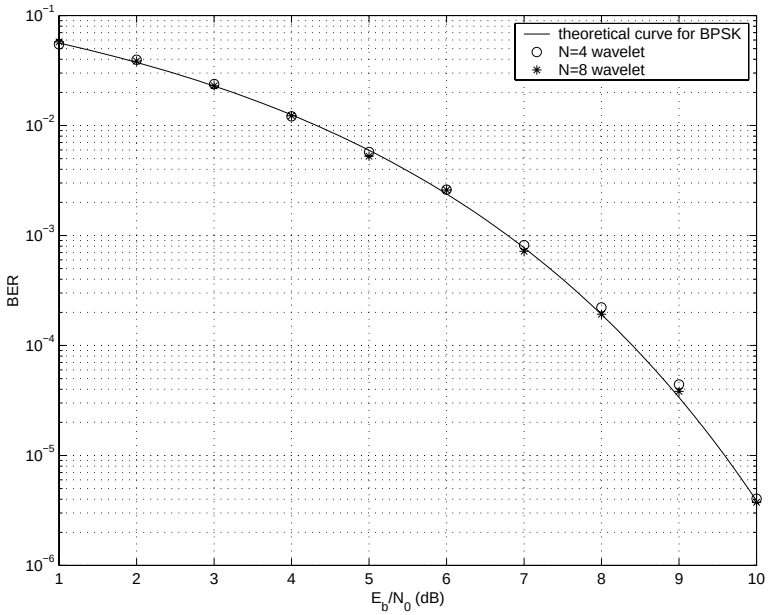

Figure 5.2: Bit Error Rate (BER) vs. E_b/N_0 of WM and BPSK in an AWGN channel. Demodulation with the Daubechies $N = 4$ and the $N = 8$ wavelets are both illustrated.

curve continues to decrease at scale 13. This improvement can be attributed to the slower fading rate of the channel at scale 13; the bit duration at scale 13 is one-eighth the duration at scale 10. Since the bit duration decreases for increasing scale, demoduation at scale 13 is less affected by the small scale fading than at scale 10 (i.e. the channel is a slower fading channel at scale 13).

Figure 5.4 illustrates similar performance of WM at scale 13 with the theoretical performance of BPSK in a flat fading channel. The performance of BPSK in a flat fading channel is given by [12]

$$P_e = \frac{1}{2}\left[1 - \sqrt{\frac{\Gamma}{1+\Gamma}}\right] \tag{5.2}$$

where $\Gamma = \frac{E_b}{N_0}\overline{\alpha^2}$ is the average value of the signal-to-noise ratio and $\overline{\alpha^2} = 1$ since the Rayleigh fading envelope is normalized. α is a random variable that represents amplitude values of

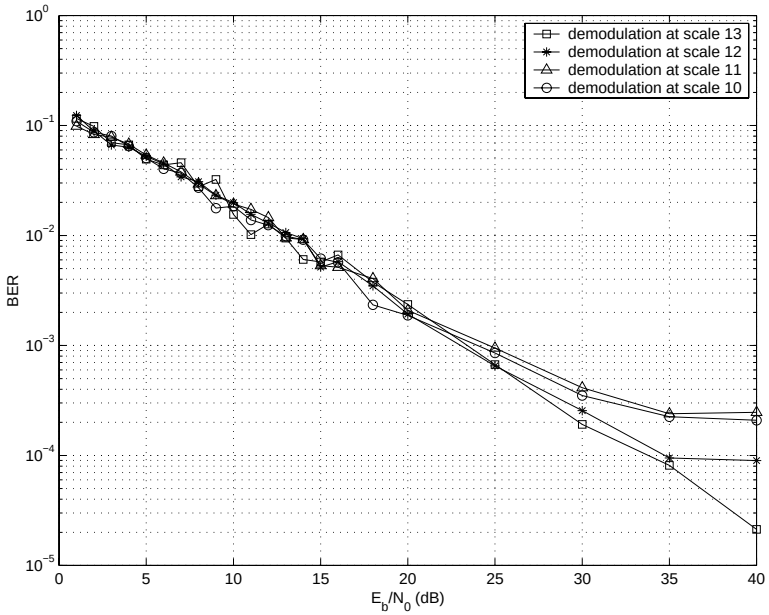

Figure 5.3: Bit Error Rate (BER) vs. E_b/N_0 in a flat fading channel with a Doppler spread of 60Hz.

the fading channel; since α is Rayleigh distributed, α^2 has a chi-square distribution.

At a given scale, the $f_d = 120$Hz channel has a faster fading rate—by a factor of two—than the $f_d = 60$Hz channel. At $E_b/N_0 > 35$dB in Figure 5.4, the BER performance of WM in the $f_d = 60$Hz channel is slightly better than the $f_d = 120$Hz channel. The error floor of WM in the 60Hz channel is lower than that in the 120Hz channel.

5.4 Performance in Frequency Selective Fading Channels

The results for the frequency selective channel show variation across scale as expected. The multirate nature of the modulation technique translates to a decrease in bit duration as

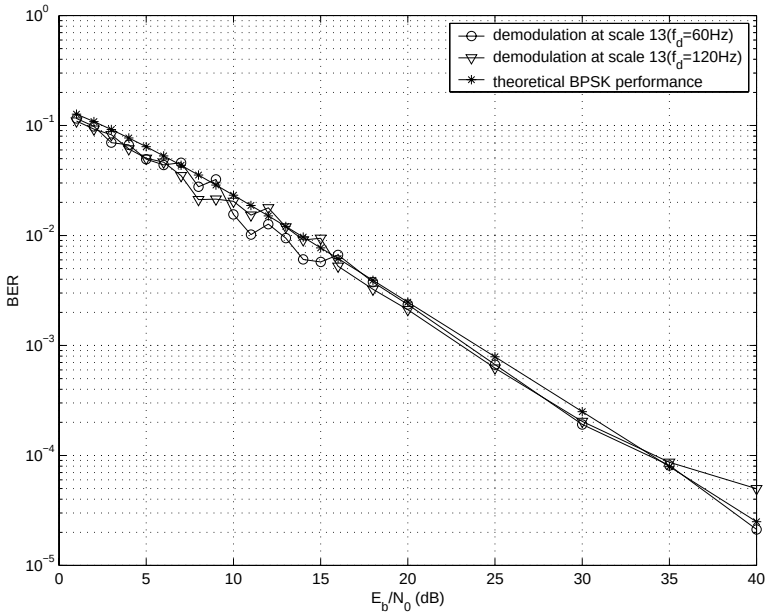

Figure 5.4: Bit Error Rate (BER) vs. E_b/N_0 in a flat fading channel with Doppler spreads of 60Hz and 120Hz. The theoretical performance of BPSK is similar to the performance of WM at scale 13 for both channels.

the scale is increased. The bit duration in relation to the delay spread (i.e. $T_s \leq 10\sigma_\tau$ for a frequency-selective channel) specifies the amount of ISI distortion observed. If the bit duration at scale 13 is $T_{S_{13}} = 2\sigma_\tau$, then the bit duration at scale 10 is $T_{S_{10}} = 8\sigma_\tau$. Therefore, the channel introduces greater distortion at scale 13 than at scale 10. Hence, a variation in performance is observed across scales.

Section 5.4.1 depicts the bit error rate performance as a function of SNR while maintaining a constant delay τ between the multipaths. Conversely, Section 5.4.2 investigates the BER performance of WM as a function of normalized delay spread while keeping SNR constant. Normalized delay spread d_i is the ratio of the rms delay spread of the channel to the period of a bit at that frequency band (i.e. $d_i = \frac{\sigma_\tau}{T_{S_i}}$ where $11 \leq i \leq 17$).

In propagation measurements by T.S. Rappaport, et. al. [15] at 900MHz, urban areas

typically had rms delays in the range of $2-3\mu s$, hilly residential areas had rms delays in the range of $5-7\mu s$ and worst case rms delay spreads were of the order of $20\mu s$. Excess delays in the range of $100\mu s$ were also observed. In Section 5.4.1 delay spreads from $1.9\mu s$ to $61\mu s$ have been used to include all cases; similary, Section 5.4.2 simulates rms delay spreads from $0.2\mu s$ to $120\mu s$.

5.4.1 Bit Error Rate vs. Signal-to-Noise ratio

The frequency selective channel described in Section 2.2.2 was implemented with two Doppler spreads: 60Hz and 120Hz. The scaling constants α_0 and α_1 in equation (2.3) were 0.707 and 0.707 respectively to give a main (carrier) ray to secondary (delayed) ray power ratio of 0dB (i.e. $\frac{E\{\alpha_0^2 ray_0(t)^2\}}{E\{\alpha_1^2 ray_1(t)^2\}} = 1$ or $C/D = 0$dB where C is the power in the main ray and D is the power in the delayed ray). The channel coefficients are normalized such that the average signal energy at the input to the channel is the same as the energy at the output. Recall that τ in equation (2.3) is $0.5T_{S_i}$, where $12 \leq i \leq 17$ (T_{S_i} refers to the bit period at scale i) and τ and σ_τ are related by $\sigma_\tau = \frac{\tau}{2}$. The rms delay spread was varied from $1.9\mu s$ ($\tau = 0.5T_{S_{17}}$) to $61\mu s$ ($\tau = 0.5T_{S_{12}}$). Coherent demodulation was performed at the receiver for all transmitted scales.

Figure 5.5 shows the BER curves for demodulation at scales 14 through 17; BPSK performance is also shown. At scale 17 the bit error rate is approximately 0.3 for all values of E_b/N_0. BER performance improves for decreasing scale: performance at scale 14 is considerably better than the performance at scale 17; the rms delay spread of $\sigma_\tau = 1.9\mu$s is comparable to the symbol period at scale 17 (i.e.$T_{S_{17}} = 7.6\mu$s); however, at scale 14 the symbol period $T_{S_{14}} = 61\mu$s, is much larger than σ_τ. Indeed at scale 14 the ISI is negligible since $T_{S_{14}} \approx 30\sigma_\tau$. The intersymbol interference (ISI) adversely impacts scales 16 and 17, but affects scale 14 to a comparatively lesser degree. Scales 14 and 15 show better performance than BPSK. This unique characteristic of WM can be exploited to obtain better BER

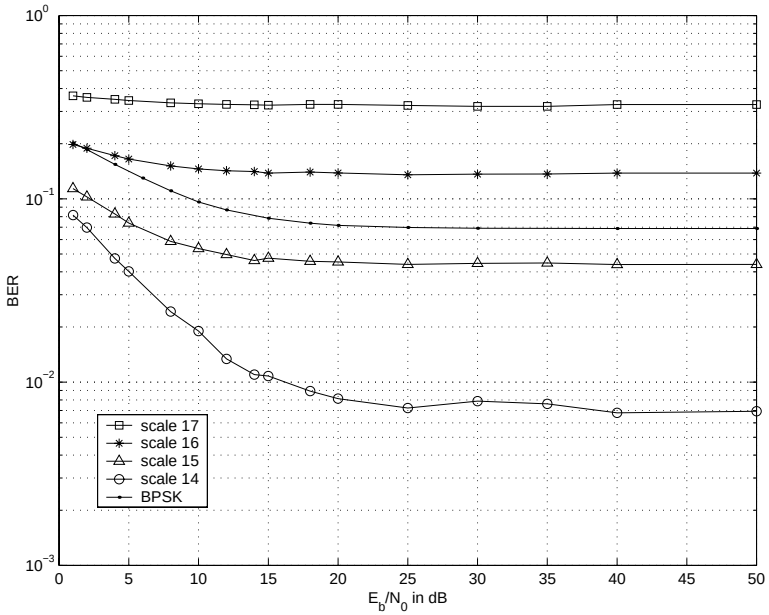

Figure 5.5: Bit Error Rate (BER) vs. E_b/N_0 in a frequency selective, slow fading channel with $f_d = 60$Hz and $\sigma_\tau = 1.9\mu s = 0.25T_{S_{17}}$ ($\tau = 0.5T_{S_{17}}$). BER performance improves for decreasing scale (scale 17 is severely distorted by intersymbol interference).

performance in mobile environments. For instance, if the worst case delay spread ($\sigma_{\tau_{max}}$) of a particular city were known, then the demodulation would be performed at the scale(s) where the channel is flattest (i.e. scales where $T_{S_i} \geq 10\sigma_{\tau_{max}}$).

Figure 5.6 shows the BER performance of WM in the frequency-selective channel for a larger value of rms delay spread for the same four scales (i.e. $\sigma_\tau = 7.6\mu s$ or $\tau = 15.2\mu s = 0.5T_{S_{15}}$). It is observed that all four scales used for the demodulation show extremely poor BER performance.

Now consider four different scales; scales 10 through 13 are transmitted over the frequency-selective channel. The rms delay spread is $15.3\mu s$ which is $0.125T_{S_{13}}$ ($\tau = 0.25T_{S_{13}}$). Figure 5.7 depicts the BER performance. Scales 10 and 11 show error floors lower than 10^{-2}. Scales 12 and 13 display significantly poorer BER performance since the ISI is larger at those scales.

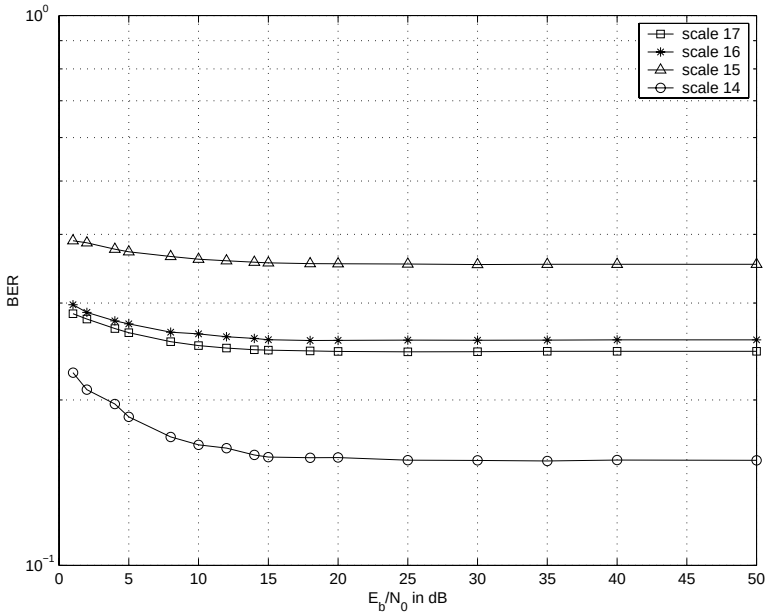

Figure 5.6: Bit Error Rate (BER) vs. E_b/N_0 in a frequency selective, slow fading channel with $f_d = 60$Hz and $\sigma_\tau = 7.6\mu s = 0.25T_{S_{15}}$ ($\tau = 0.5T_{S_{15}}$). BER performance improves for decreasing scale (all scales are distorted by intersymbol interference; however, scale 14 performs the best).

Figure 5.8 shows the BER performance of scales 10 through 13 when the rms delay spread is $30.5\mu s = 0.25T_{S_{13}}$ ($\tau = 0.5T_{S_{13}}$). All scales indicate poor BER performance when compared to Figure 5.7 where $\sigma_\tau = 15.3\mu s$. This is expected since the rms delay spread is lower for the channel in Figure 5.7. A comparison of Figures 5.5 and 5.8—where the rms delay spread is one-fourth the bit period of the highest scale at which demodulation is performed—reveals similar performance. Scales 11 through 13 show the same error floor as scales 15 through 17 and scale 14 shows slightly better performance when compared to scale 10.

Further simulations were performed for larger rms delay spreads. Figure 5.9 shows the BER performance for all scales when the rms delay spread is $0.25T_{S_{12}}$ ($\tau = 0.5T_{S_{12}}$). In Figure 5.9, scales 11, 12 and 13 perform poorly while scale 10 shows a slightly better performance.

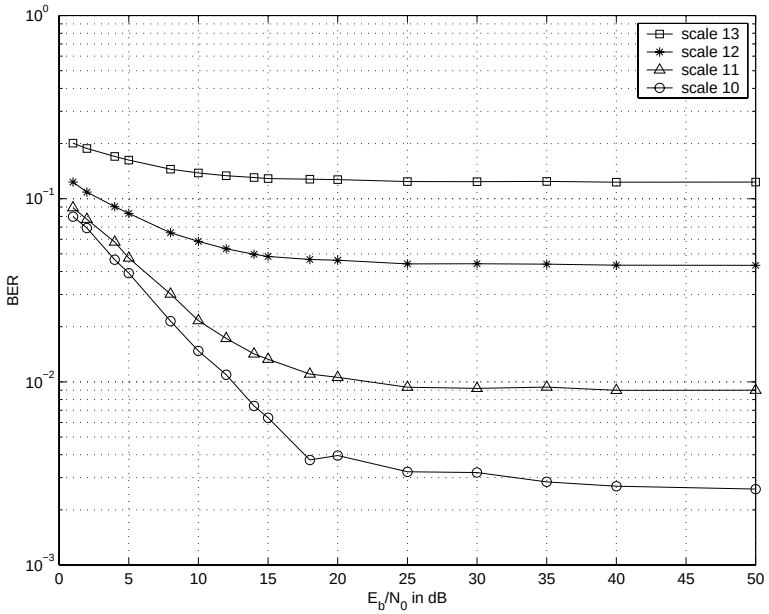

Figure 5.7: Bit Error Rate (BER) vs. E_b/N_0 in a frequency selective, slow fading channel with $f_d = 60$Hz and $\sigma_\tau = 15.3\mu s = 0.125T_{S_{13}}$ ($\tau = 30.5\mu s = 0.25T_{S_{13}}$). BER performance improves for decreasing scale (scale 13 is severely distorted by intersymbol interference).

Furthermore, scale 13 has a lower error floor than scale 12.

On comparing Figures 5.7 through 5.9, a gradual degradation of performance is seen for scale 10 demodulation as the delay τ is increased; scale 10 shows the best performance in Figure 5.7 (i.e. for $\sigma_\tau = 0.125T_{S_{13}}$) and the worst performance in Figure 5.9 (i.e. for $\sigma_\tau = 0.25T_{S_{12}}$). This is due to the increase in ISI for scale 10 data as the delay between the paths is gradually increased. At $\sigma_\tau = 0.25T_{S_{12}}$ (Figure 5.9), the second ray is delayed by half a symbol at scale 12 resulting in the distortion of the received signal at that scale and at scale 10 (due to ISI) from which the receiver cannot recover.

Furthermore, it is observed that the number of scales that can be used for demodulation—assuming a minimum BER of 10^{-2}—decreases as the value of τ is increased. In particular, for $\tau = 0.25T_{S_{13}}$ (Figure 5.7), scales 10 and 11 can be used for demodulation, but for $\tau = 0.5T_{S_{13}}$

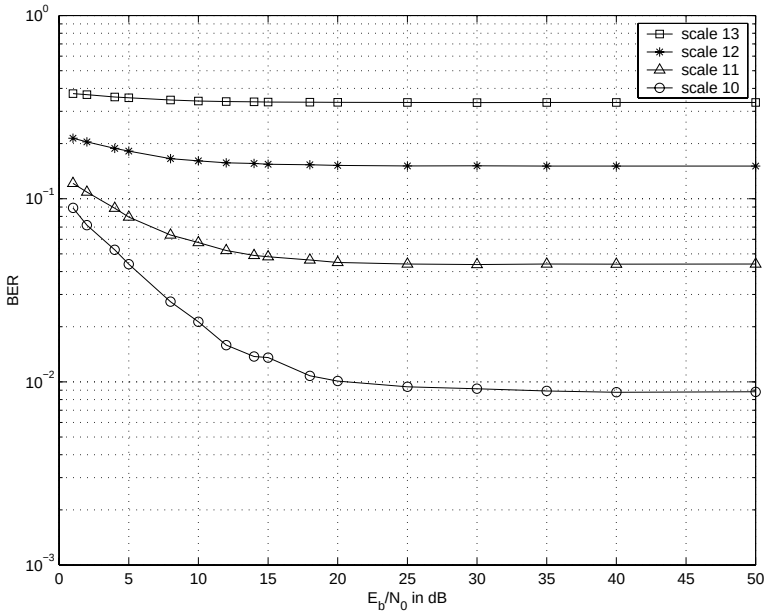

Figure 5.8: Bit Error Rate (BER) vs. E_b/N_0 in a frequency selective, slow fading channel with $f_d = 60$Hz and $\sigma_\tau = 30.5\mu s = 0.25T_{S_{13}}$ ($\tau = 0.5T_{S_{13}}$).

(Figure 5.8), only scale 10 can be used for demodulation. Hence, an intelligent selection of demodulation scales at the receiver can result in superior BER performance. Our method to determine which scales can be used for demodulation was described in Section 4.2; these results are depicted in Section 5.7.

The channel parameters are varied to obtain an $f_d = 120$Hz frequency-selective channel. Figure 5.10 shows the performance of WM in the 120Hz frequency-selective channel for $\sigma_\tau = 0.25T_{S_{13}}$ ($\tau = 0.5T_{S_{13}}$). Comparing Figures 5.8 and 5.10, scales 10 through 13 show similar performance in both channels; even for high values of E_b/N_0. Since the results for the 120Hz channel do not vary appreciably from that which was observed for the 60Hz channel, it can be concluded that the limit on the BER is due to the ISI in a frequency-selective channel.

The main ray to secondary ray power ratio is changed such that $C/D = 10$dB and the delay

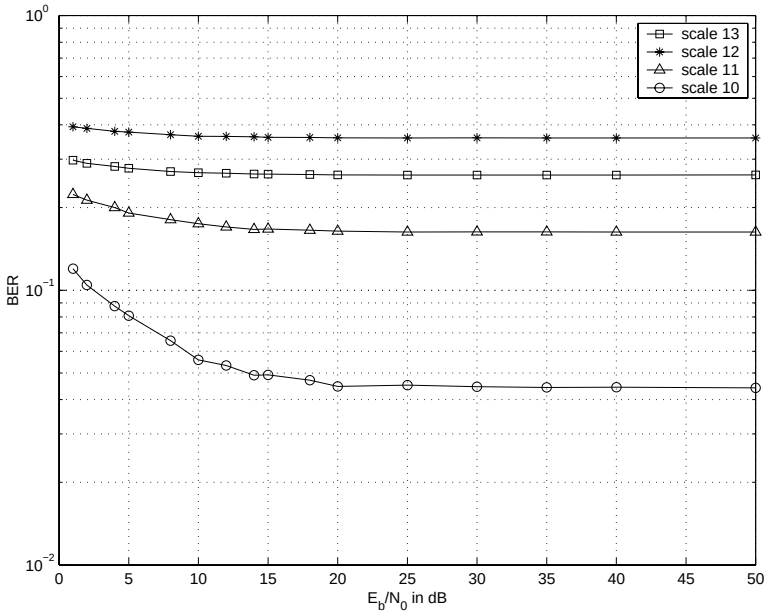

Figure 5.9: Bit Error Rate (BER) vs. E_b/N_0 in a frequency selective, slow fading channel with $f_d = 60$Hz and $\sigma_\tau = 61\mu s = 0.25T_{S_{12}}$ ($\tau = 0.5T_{S_{12}}$). Scale 10 performs slightly better than the other scales.

between the main ray and the secondary ray $\tau = 61\mu s$ ($\sigma_\tau = 18\mu s \neq \frac{\tau}{2}$). Figure 5.11 shows the performance of WM in this channel. It is seen that the error floor for scale 10 is the same as in Figure 5.10; however, scales 11, 12 and 13 have a lower error floor than in Figure 5.10 where C/D was 0dB. This behavior is as expected, since the ISI caused by the secondary ray has decreased by a factor of 10 (i.e. the secondary ray has 10 times less power than the primary ray).

5.4.2 Bit Error Rate vs. Normalized Delay Spread

In the previous section, performance was measured as a function of E_b/N_0 with a constant rms delay spread for each BER curve. In this section, the E_b/N_0 value is fixed at 50dB and

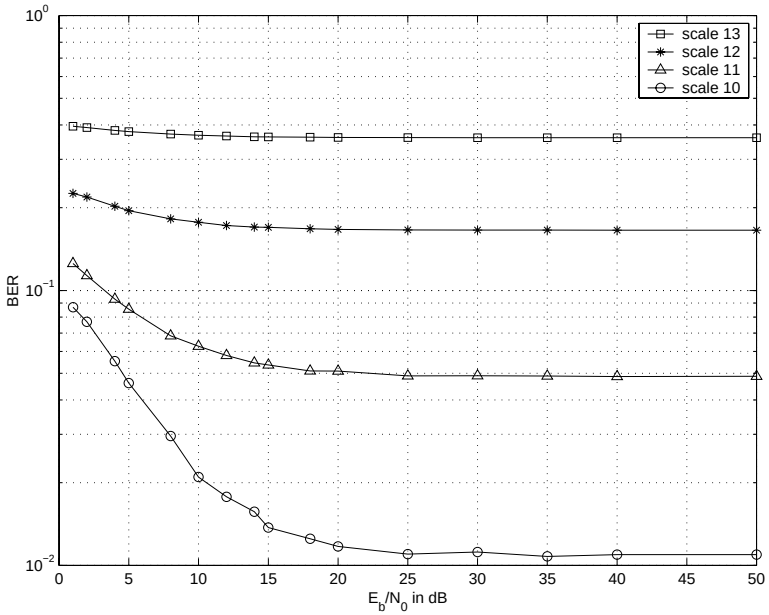

Figure 5.10: Bit Error Rate (BER) vs. E_b/N_0 in a frequency selective, slow fading channel with $f_d = 120$Hz and $\sigma_\tau = 30.5\mu s = 0.25T_{S_{13}}$ ($\tau = 61\mu s = 0.5T_{S_{13}}$).

the rms delay spread σ_τ is varied from $0.2\mu s$ to $120\mu s$; this variation in rms delay spread shows the effect of ISI on demodulation performance for each scale. For these simulations, $\alpha_0 = \alpha_1 = 0.707$. This results in a main-path to delayed-path power ratio of one (i.e. $\frac{E\{\alpha_0^2 ray_0(t)^2\}}{E\{\alpha_1^2 ray_1(t)^2\}} = 1$ or $C/D = 0$dB where C is the power in the main ray and D is the power in the delayed ray). The rms delay spread, σ_τ, is normalized to the symbol period at each scale (i.e. normalized delay spread at each scale is given by $d_i = \frac{\sigma_\tau}{T_{S_i}}$ where $11 \leq i \leq 17$). The Doppler spread used is $f_d = 120$Hz.

Figure 5.12 is a plot of BER vs. normalized rms delay spread; d_{13} is normalized with respect to scale 13 (i.e. $d_{13} = \frac{\sigma_\tau}{T_{S_{13}}} = \frac{\tau}{2T_{S_{13}}}$). $T_{S_{13}}$ remains constant while σ_τ varies. As σ_τ increases, the amount of ISI increases; thus, for all scales there is an increase in bit error rate as d_{13} increases. As σ_τ decreases, the amount of ISI decreases; thus, for all scales there is a drop in bit error rate as d_{13} decreases. When $d_{13} = 0.25$, then ISI is on the order of scale 13 (since $\sigma_\tau = \frac{T_{S_{13}}}{4}$; $d_{13} = 0.25$). The performance of all scales at $d_{13} = 0.25$ matches the

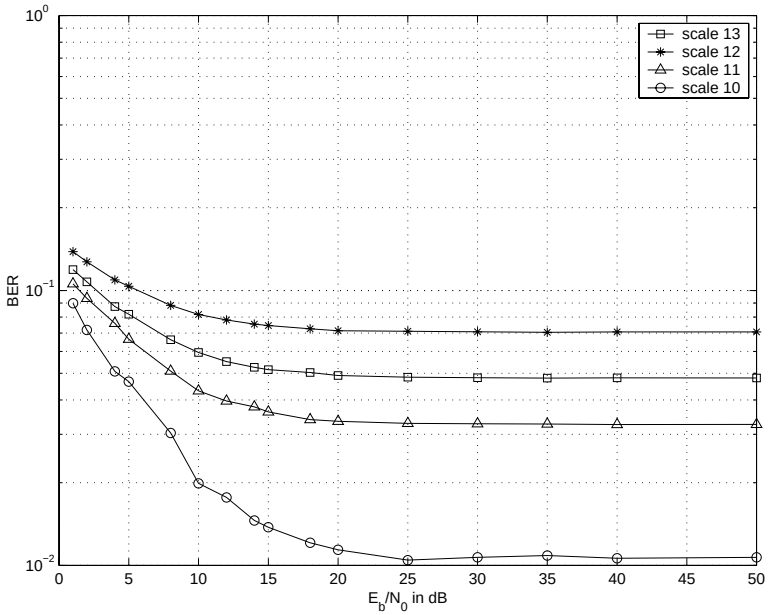

Figure 5.11: Bit Error Rate (BER) vs. E_b/N_0 in a frequency selective, slow fading channel with $f_d = 120$Hz and $\tau = 61\mu s = 0.5T_{S_{13}}$ and $C/D = 10$dB. Improved BER performance is seen for scales 11, 12 and 13 when the power in the main ray is increased by a factor of 10.

BER performance in Figure 5.10 at $E_b/N_0 = 50$dB. Demodulation at scale 13 performs the worst while demodulation at scale 10 performs the best. The performance improves with decreasing scale; this is expected since the ISI decreases as we go to lower scales.

Figure 5.12 also indicates that scales 10 and 11 perform better than BPSK for most values of normalized delay spread. This shows the performance improvement that can be realized by using scale 10 data for demodulation when the rms delay spread is of the order of the bit period at scale 13.

Figure 5.13 is a plot of BER vs. normalized rms delay spread; d_{12} is normalized with respect to scale 12 (i.e. $d_{12} = \frac{\sigma_\tau}{T_{S_{12}}} = \frac{\tau}{2T_{S_{12}}}$). $T_{S_{12}}$ remains constant while σ_τ varies. As σ_τ increases, the amount of ISI increases; thus, for all scales there is an increase in bit error rate as d_{12} increases. As σ_τ decreases, the amount of ISI decreases; thus for all scales there is a drop

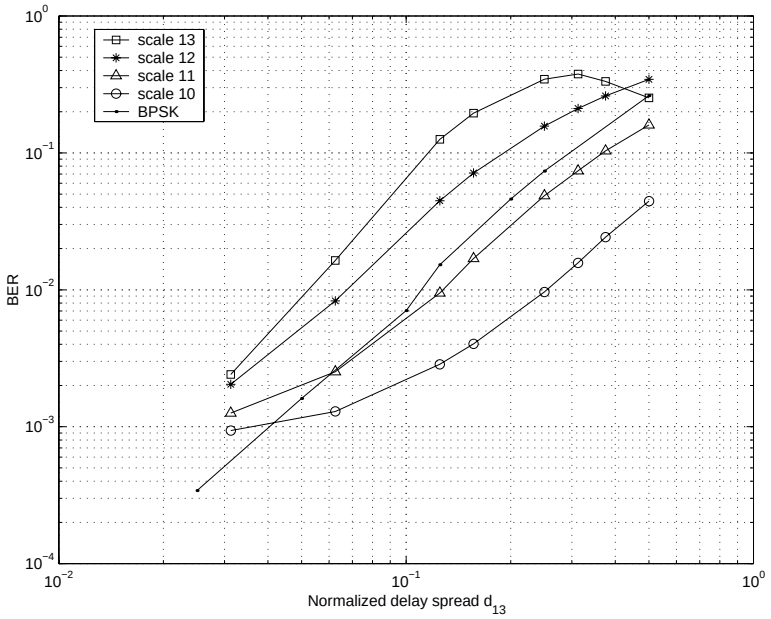

Figure 5.12: BER performance vs. normalized delay spread $d_{13} = \frac{\sigma_\tau}{T_{S_{13}}}$ ($\sigma_\tau \in [3.66\mu s, 61\mu s]$). BER performance of BPSK is also shown. Scale 10 shows the best performance at all values of delay spread. Performance at scales 10 and 11 is observed to be better than BPSK for almost all values of d_{13}.

in bit error rate as d_{12} decreases. When $d_{12} = 0.25$, then ISI is on the order of scale 12 (since $\sigma_\tau = \frac{T_{S_{12}}}{4}$; $d_{12} = 0.25$). The performance of all scales at $d_{12} = 0.25$ matches the BER performance in Figure 5.9 at $E_b/N_0 = 50$dB. The trend from Figure 5.12 continues; demodulation at scale 13 performs the worst while demodulation at scale 10 performs the best. The performance improves with decreasing scale; this is expected since the ISI decreases as we go to lower scales.

Figure 5.13 also indicates that scale 10 performs better than BPSK for most values of normalized delay spread. This shows the performance improvement that can be realized by using scale 10 data for demodulation when the rms delay spread is of the order of the bit period at scale 12.

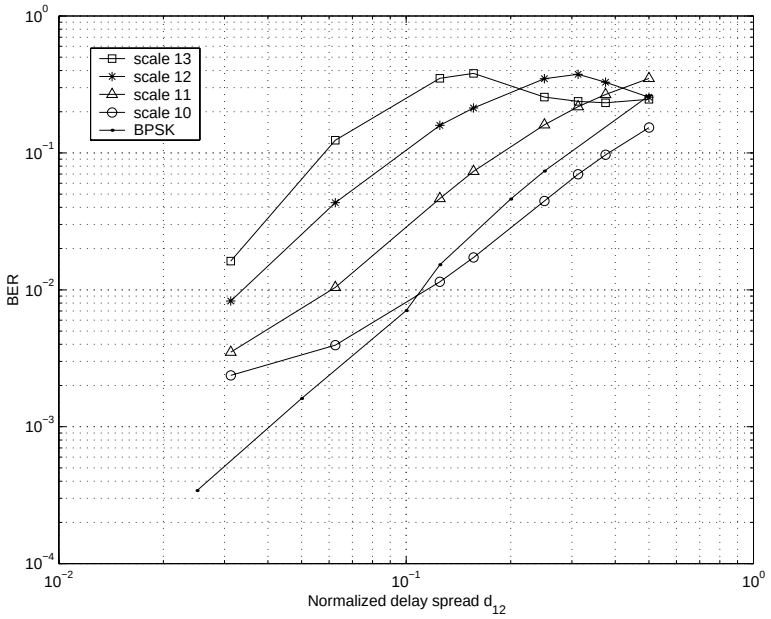

Figure 5.13: BER performance vs. normalized delay spread $d_{12} = \frac{\sigma_\tau}{T_{S_{12}}}$. Scale 10 performs the best at all values of delay spread. BPSK performance is also shown.

Figure 5.14 is a plot of BER vs. normalized rms delay spread; d_{11} is normalized with respect to scale 11 (i.e. $d_{11} = \frac{\sigma_\tau}{T_{S_{11}}} = \frac{\tau}{2T_{S_{11}}}$). $T_{S_{11}}$ remains constant while σ_τ varies. As σ_τ increases, the amount of ISI increases; thus, for all scales there is an increase in bit error rate as d_{11} increases. For values of $d_{11} > 0.2$, all scales depict poor performance. As σ_τ decreases, the amount of ISI decreases; thus, for all scales there is a drop in bit error rate as d_{11} decreases. Demodulation at scale 13 performs the worst while demodulation at scale 10 performs the best. The performance improves with decreasing scale; this is expected since the ISI decreases as we go to lower scales. The performance of all scales is poorer when compared to Figures 5.12 and 5.13; this is due to the larger ISI experienced by all scales ($d_{11} = \frac{\sigma_\tau}{T_{S_{11}}}$ and $T_{S_{11}} = 4T_{S_{13}}$).

Figure 5.15 is a plot of BER vs. normalized rms delay spread d_{17}; d_{17} is normalized with respect to scale 17 (i.e. $d_{17} = \frac{\sigma_\tau}{T_{S_{17}}} = \frac{\tau}{2T_{S_{17}}}$). Scales 14 thorugh 17 are transmitted. It is observed that the performance observed in Figure 5.15 is the same as in Figure 5.12.

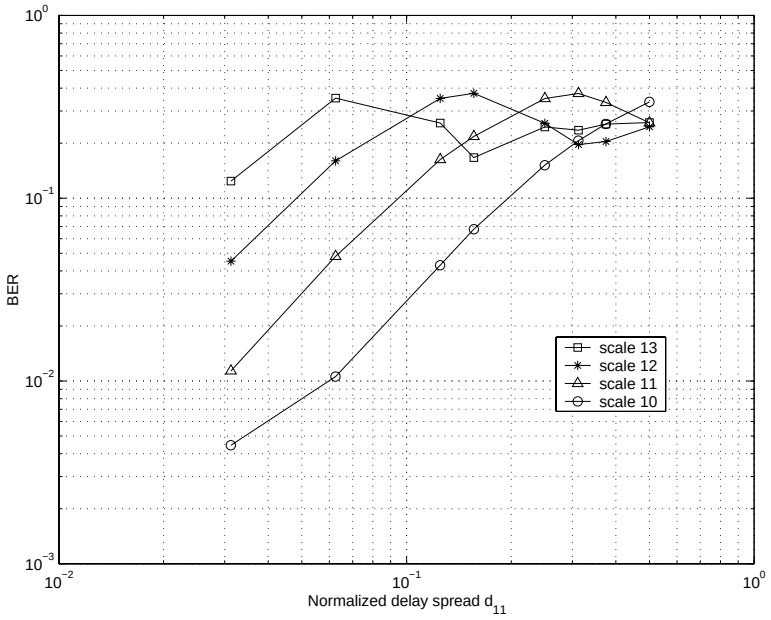

Figure 5.14: BER performance vs. normalized delay spread $d_{11} = \frac{\sigma_\tau}{T_{S_{11}}}$. All scales perform poorly; scale 10 depicts best performance.

The equivalent scales show similar BER performance; scale 14 shows slightly better BER performance at $d_{17} = 0.03$. This is attributed to the impact of the slower fading channel for scale 14 data. When $d_{17} = 0.25$, then ISI is on the order of scale 17 (since $\sigma_\tau = \frac{T_{S_{17}}}{4}$; $d_{17} = 0.25$). The performance of all scales at $d_{17} = 0.25$ matches the BER performance in Figure 5.5 at $E_b/N_0 = 50$dB.

5.5 Channel Performance Comparison

Figure 5.16 compares the BER curve for the 3 channel types at scales 10 and 13 and $f_d = 60$Hz (AWGN is shown only for scale 10 since all scales gave nearly identical results). For the frequency-selective channel, $\sigma_\tau = 15.3\mu s = \frac{T_{S13}}{8}$. WM experiences the best BER performance in the AWGN channel; it is identical to the BER performance of BPSK in an AWGN channel.

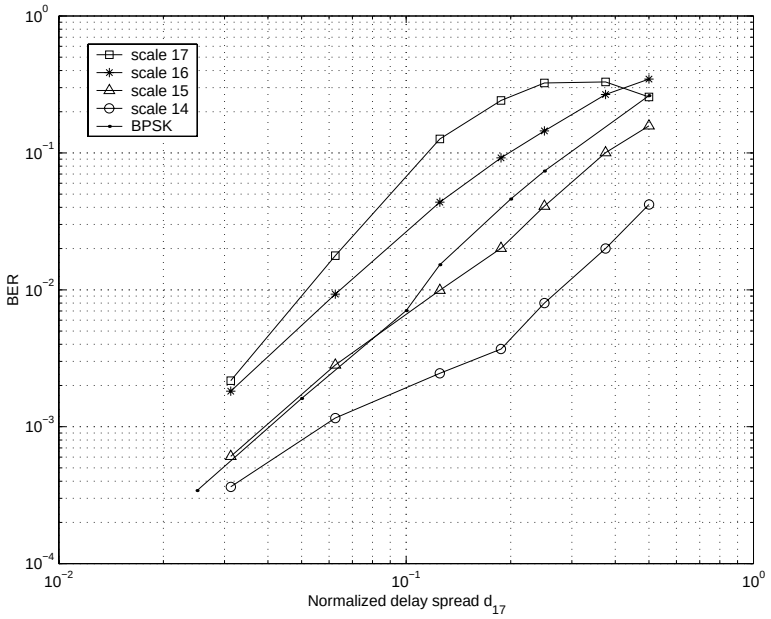

Figure 5.15: BER performance vs. normalized delay spread $d_{17} = \frac{\sigma_\tau}{T_{S_{17}}}$. Scale 14 shows better performance than BPSK for all values of normalized delay spread.

At scale 10 (i.e. low value of ISI), the flat fading channel gives better performance than the frequency-selective fading channel. This is because of the presence of the secondary (undesired) multipath component in the frequency-selective channel, which, if not in phase with the primary component will result in errors.

On the other hand, for scale 13, the BER performance of the flat fading channel is significantly better than the frequency selective channel. At scale 13 the frequency selective channel is severely distorted by ISI.

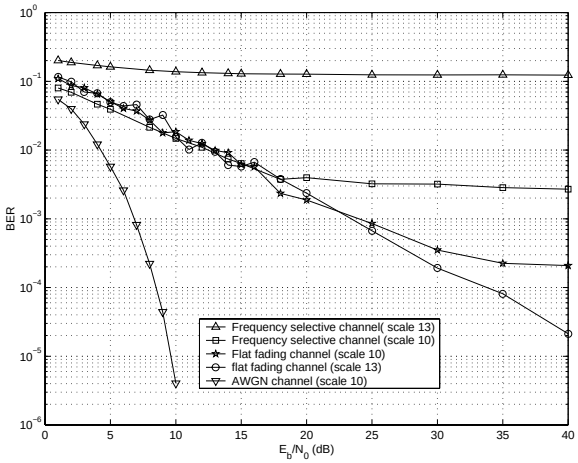

Figure 5.16: Bit Error Rate (BER) vs. E_b/N_0 in the AWGN, frequency selective and flat fading channels with $f_d = 60$Hz. For the frequency-selective channel, $\sigma_\tau = 15.3\mu s = \frac{T_{S13}}{8}$. WM in the AWGN channel gives the best performance. Results for the flat fading channel are better than the results for the frequency selective channel at all scales.

5.6 Joint Statistic Results

Sections 5.1 through 5.5 examined WM performance using a single copy of the data at a particular scale. However, WM transmits data at multiple rates; this redundancy can be exploited to improve the bit error rate performance. We now illustrate our joint statistic method described in Chapter 4, Section 4.1. The simulations were performed for the AWGN channel, the Rayleigh flat fading channel ($f_d = 60$Hz), and the frequency-selective channel at $f_d = 60$Hz.

5.6.1 AWGN Channel

Figure 5.17 shows the BER performance when K=1, 2, 3, 4 and 7 observations are used for estimation of the received bit. Theoretical BER performance using the joint estimation

strategy outlined in Section 4.1 for the AWGN channel is given by [19]

$$P_e = \mathrm{Q}(\sqrt{\frac{2KE_b}{N_0}}) \tag{5.3}$$

where K is the redundancy factor.

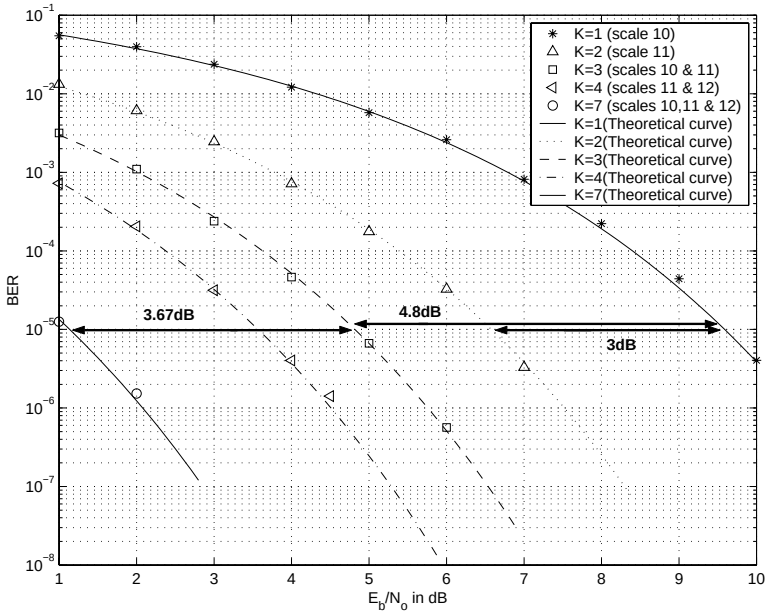

Figure 5.17: BER vs. E_b/N_0 in an AWGN channel using joint estimation at the receiver. The number of copies is $K = 1$, 2, 3, 4 and 7. At $P_e = 10^{-5}$, the performance gain resulting from joint estimation when $K = 3$ is 4.8dB, for $K = 7$, the gain achieved is 8.47dB.

For $K = 2$, two observations from scale 11 were used. For $K = 3$, one observation at scale 10 and two observations at scale 11 were used (and so forth for $K = 4$ and 7). Figure 5.17 shows that the simulated data matches the theoretical curves. A 4.8dB performance gain is realized at $P_e = 10^{-5}$ when three observations are used instead of one; for the same value of P_e, a gain of 8.47dB is observed when seven observations are used instead of one. These performance

improvements are achieved by exploiting the inherent redundancy of WM. Notice that these improvements correspond to $10logK$ dB (e.g. $10log(7) = 8.45$dB). In other words, this use of 7 data copies in WM results in performance equivalent to BPSK with a 7-fold increase in SNR.

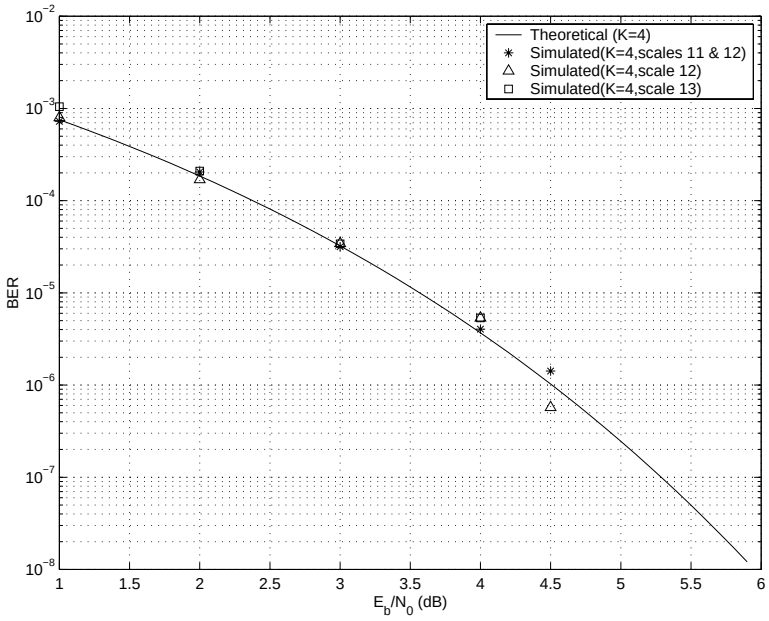

Figure 5.18: BER vs. E_b/N_0 in an AWGN channel using joint estimation at the receiver. $K = 4$ observations from different scales are used in each case.

Figure 5.18 shows the theoretical and simulated BER results for $K = 4$ observations. The figure contains three simulated curves; each of the simulated curves uses observations from different scales. First, the observations are from scales 11 and 12, next from scale 12 only, and finally, from scale 13 only. All the three cases closely match the theoretical curve for $K = 4$. This observation allows us to conclude that for the AWGN channel, the performance gain is independent of the scale(s) from which the observations are used.

5.6.2 Flat Fading Channel

Figure 5.19 shows the simulated curves for joint estimation performed at the receiver when the channel is a slow, flat Rayleigh fading channel ($f_d = 60$Hz). The performance gain when K increases from 1 to 2 is 18dB; gains of 25db and 32dB are realized as K increases from 1 to 3 and 1 to 7, respectively. BPSK is equivalent to the $K = 1$ curve. Viewed another way, to obtain a bit error rate of 10^{-4}, an E_b/N_0 of 17dB is required when 2 observations are used compared to 35dB when only a single observation is used. Notice that these improvements are much larger than $10logK$ dB. Unlike the AWGN channel, WM outperforms BPSK given the same increase in SNR. This large improvement could be translated into increased talk time for mobile terminals (since their power source is limited by the life of the battery).

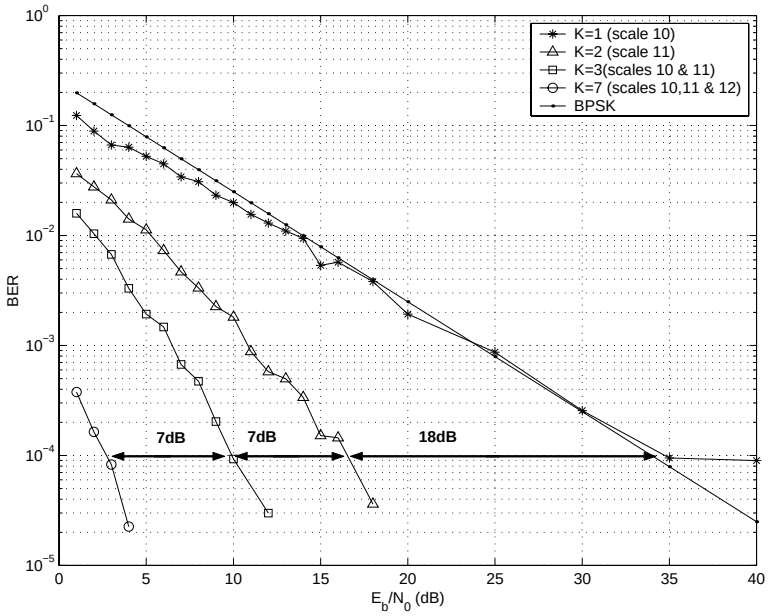

Figure 5.19: BER vs. E_b/N_0 in a Rayleigh flat fading channel at $f_d = 60$Hz using joint estimation at the receiver. K takes values 1, 2, 3 and 7. At $P_e = 10^{-4}$, the performance gain obtained due to joint estimation when $K = 2$ is 18dB, $K = 3$ is 25dB and for $K = 7$, the gain obtained is 32dB. BPSK performance in the flat fading channel is also shown.

5.6.3 Frequency-Selective Fading Channels

Figure 5.20 illustrates BER performance of WM in a frequency-selective channel at $f_d = 60$Hz with a delay of $\tau = 30.5\mu s$ ($\sigma_\tau = 15.3\mu s$). Scale 13 is most corrupted by ISI; scale 10 is least corrupted. Multiple noisy observations are used to obtain an estimate of the received bit; $K = 2$, 3 and 4 observations from different scales are used to obtain the curves shown in Figure 5.20. $K = 3$ shows the best performance since scale 10 and 11 data is used to obtain the estimate. The $K = 4$ curve shows poor performance even though more observations are used to arrive at this estimate. This is attributed to the inclusion of scale 12 and scale 13 data in the calculation of the joint statistic; scales 12 and 13 experience large ISI and show poor BER performance.

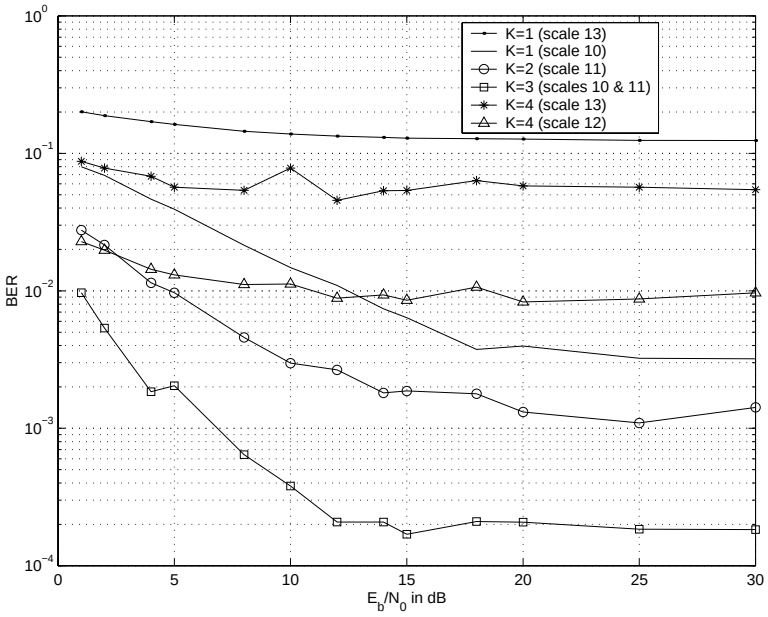

Figure 5.20: BER performance in frequency-selective fading channel at $f_d = 60$Hz using $K = 1$, 2, 3 and 4 observations. The $K = 3$ curve gives the best performance followed by the $K = 2$ curve. The $K = 4$ curve for scale 13 data performs poorly when compared to the $K = 4$ curve for scale 12 data.

For $K = 4$, two simulations have been performed with noisy observations from scales 12 and 13. For noisy observations taken from scale 12, the estimate showed better BER performance than for observations used from scale 13. This is expected, since the data at scale 13 is corrupted to a larger extent by ISI. A combination of scale 12 data and scale 13 data is also used for determining the estimate. This curve shows an improvement over the $K = 4$ estimate using scale 13 data, but performs poorer than the $K = 4$ estimate obtained using scale 12 data. Curves using one copy of the data at scales 10 and 13 have been shown. The $K = 2$ and $K = 3$ curves show better performance than when demodulation is done using only one copy at any of the scales. The $K = 4$ curve using observations from scale 13 performs better than the $K = 1$ curve at scale 13. Therefore, the use of a joint statistic for estimation always gives better results than when only one copy is used.

5.7 Channel Identification Results

The ANOVA analysis for channel identification described in Chapter 4, Section 4.2 was performed for numerous trials. Each channel was examined at two SNRs.

The AWGN channel was examined at $E_b/N_0 = 4$dB and $E_b/N_0 = 8$dB. Tables 5.1 and 5.2 show the computed F-statistics. In all 20 trials, the F-statistic was below $F_0 = 2.6$. Thus, the null hypothesis H_0 is accepted at the 0.05 significance level and all of the channels are correctly identified as AWGN. Furthermore, the F statistic was observed to be less than 1.5 (the threshold separating AWGN and flat fading channels). A 100% success rate was obtained for AWGN channel identification.

For the Rayleigh fading channel at 60Hz, 10 trials were conducted at $E_b/N_0 = 10$dB and also at $E_b/N_0 = 30$dB. Tables 5.3 and 5.4 depict the computed F statistics. In 18 out of 20 trials, H_0 is rejected in favor of H_1 at the 0.05 significance level. For the 2 accept H_0 cases (trial 10 in Table 5.3 and trial 6 in Table 5.4), the F statistic is greater than

Table 5.1: ANOVA results for AWGN channel at $E_b/N_0 = 4$dB.

Trial	F	H_0	Channel ID
1	0.37	Accept	AWGN
2	1.02	Accept	AWGN
3	1.42	Accept	AWGN
4	0.33	Accept	AWGN
5	0.47	Accept	AWGN
6	0.49	Accept	AWGN
7	0.62	Accept	AWGN
8	1.34	Accept	AWGN
9	0.49	Accept	AWGN
10	0.90	Accept	AWGN

$F_1 = 1.5$ (threshold between the AWGN and flat fading) for only 1 trial. Thus trial 6 at $E_b/N_0 = 30dB$ is correctly identified as a flat fading channel, but trial 10 at $E_b/N_0 = 10dB$ is incorrectly identified as AWGN. For the 18 reject H_0 cases, the F statistic is lower than $F_2 = 13$ (threshold between the flat fading and frequency-selective fading). Thus, all 18 trials are correctly identified as flat fading channels. Overall, a 95% success rate for flat fading channel identification was realized.

In the frequency-selective channel, there is a large variation in the data statistics across scale. Thus, the computed F-statistics are typically very large at both SNR levels ($E_b/N_0 = 12$dB and $E_b/N_0 = 30$dB). Tables 5.5 and 5.6 depict the computed F statistics. In all 20 trials, the F statistic is greater than $F_0 = 3.78$; thus, the null hypothesis H_0 is rejected in favor of H_1 at a 0.01 significance level. Furthermore, the F values are all larger than $F_2 =$

Table 5.2: ANOVA results for AWGN channel at $E_b/N_0 = 8$dB.

Trial	F	H_0	Channel ID
1	0.68	Accept	AWGN
2	0.18	Accept	AWGN
3	1.44	Accept	AWGN
4	0.89	Accept	AWGN
5	0.02	Accept	AWGN
6	1.30	Accept	AWGN
7	1.49	Accept	AWGN
8	1.24	Accept	AWGN
9	0.36	Accept	AWGN
10	1.00	Accept	AWGN

13 (the threshold separating flat fading and frequency-selective channels) and all channels are correctly identified as frequency-selective. A 100% success rate for frequency-selective channel identification was obtained.

Unlike AWGN and flat fading channels where all scales can be used for demodulation, the scales that should be used for demodulation in a frequency-selective channel are those that are least corrupted by ISI. In a frequency-selective channel, the scale with the minimum mean value is the scale at which τ is of the order of the bit period and ISI effects are most severe (i.e. $\tau = \frac{T}{2}$ or $\tau = \frac{T}{4}$). In our algorithm described in Chapter 4, Section 4.2, if scale N is the most corrupted scale, scales $N-2$ and lower should be used for demodulation. It should be noted that these trials simulate rms delay spreads ranging from $1.9\mu s$ to $61\mu s$. These trials do not take into account the behavior of this channel for values of τ greater

Table 5.3: ANOVA results for Rayleigh flat fading channel at 60Hz for $E_b/N_0 = 10$dB.

Trial No.	F	H_0	Channel ID
1	3.83	Reject	Flat Fading
2	2.82	Reject	Flat Fading
3	3.35	Reject	Flat Fading
4	3.90	Reject	Flat Fading
5	4.31	Reject	Flat Fading
6	2.94	Reject	Flat Fading
7	11.62	Reject	Flat Fading
8	3.32	Reject	Flat Fading
9	3.61	Reject	Flat Fading
10	1.01	Accept	AWGN

than $\frac{T_{S_{12}}}{2}$, since delay spreads greater than $61\mu s$ are not typically observed in the field [15].

Table 5.6 shows the F statistic, the channel type, the scale with the minimum mean, and the scales that should be used for demodulation for different values of τ. Consequently, our algorithm correctly deduces which scales should be used for demodulation 100% of the time. Consider trials 13 through 16 in Tables 5.5 and 5.6; τ is of the order of scale 13 ($\tau = \frac{T_{S_{13}}}{2}$) and scales 10 and 11 should be used for demodulation. Figure 5.21 shows the improved BER performance obtained at the receiver when scales 10 and 11 are both used.

We have illustrated our method that successfully identifies the channel type and rms delay spread and shown how demodulation performance can be improved.

Table 5.4: ANOVA results for Rayleigh flat fading channel at 60Hz for $E_b/N_0 = 30$dB.

Trial No.	F	H_0	Channel ID
1	3.34	Reject	Flat Fading
2	6.57	Reject	Flat Fading
3	3.49	Reject	Flat Fading
4	10.84	Reject	Flat Fading
5	2.72	Reject	Flat Fading
6	1.61	Accept	Flat Fading
7	3.74	Reject	Flat Fading
8	2.71	Reject	Flat Fading
9	7.07	Reject	Flat Fading
10	6.44	Reject	Flat Fading

Table 5.5: ANOVA results for frequency-selective fading channel at 60Hz for $E_b/N_0 = 12$dB.

Trial No.	τ	F	H_0	Channel ID	low mean scale	Demodulation scales ID
1	$0.5T_{S_{17}}$	34.30	Reject	Frequency-selective	17	14, 15
2	$0.5T_{S_{17}}$	131.45	Reject	Frequency-selective	17	14, 15
3	$0.5T_{S_{17}}$	142.86	Reject	Frequency-selective	17	14, 15
4	$0.5T_{S_{17}}$	99.35	Reject	Frequency-selective	17	14, 15
5	$0.5T_{S_{15}}$	32.33	Reject	Frequency-selective	15	none
6	$0.5T_{S_{15}}$	30.37	Reject	Frequency-selective	15	none
7	$0.5T_{S_{15}}$	47.17	Reject	Frequency-selective	15	none
8	$0.5T_{S_{15}}$	44.32	Reject	Frequency-selective	15	none
9	$0.25T_{S_{13}}$	25.01	Reject	Frequency-selective	13	10, 11
10	$0.25T_{S_{13}}$	82.34	Reject	Frequency-selective	13	10, 11
11	$0.25T_{S_{13}}$	59.33	Reject	Frequency-selective	13	10, 11
12	$0.25T_{S_{13}}$	77.12	Reject	Frequency-selective	13	10, 11
13	$0.5T_{S_{13}}$	261.48	Reject	Frequency-selective	13	10, 11
14	$0.5T_{S_{13}}$	71.51	Reject	Frequency-selective	13	10, 11
15	$0.5T_{S_{13}}$	56.75	Reject	Frequency-selective	13	10, 11
16	$0.5T_{S_{13}}$	69.23	Reject	Frequency-selective	13	10, 11
17	$0.5T_{S_{12}}$	17.00	Reject	Frequency-selective	12	10
18	$0.5T_{S_{12}}$	45.96	Reject	Frequency-selective	12	10
19	$0.5T_{S_{12}}$	46.51	Reject	Frequency-selective	12	10
20	$0.5T_{S_{12}}$	34.80	Reject	Frequency-selective	12	10

Table 5.6: ANOVA results for frequency-selective fading channel at 60Hz for $E_b/N_0 = 30$dB.

Trial No.	τ	F	H_0	Channel ID	low mean scale	Demodulation scales ID
1	$0.5T_{S_{17}}$	93.95	Reject	Frequency-selective	17	14, 15
2	$0.5T_{S_{17}}$	25.99	Reject	Frequency-selective	17	14, 15
3	$0.5T_{S_{17}}$	122.24	Reject	Frequency-selective	17	14, 15
4	$0.5T_{S_{17}}$	50.68	Reject	Frequency-selective	17	14, 15
5	$0.5T_{S_{15}}$	38.15	Reject	Frequency-selective	15	none
6	$0.5T_{S_{15}}$	113.46	Reject	Frequency-selective	15	none
7	$0.5T_{S_{15}}$	35.09	Reject	Frequency-selective	15	none
8	$0.5T_{S_{15}}$	66.11	Reject	Frequency-selective	15	none
9	$0.25T_{S_{13}}$	28.27	Reject	Frequency-selective	13	10, 11
10	$0.25T_{S_{13}}$	52.25	Reject	Frequency-selective	13	10, 11
11	$0.25T_{S_{13}}$	34.01	Reject	Frequency-selective	13	10, 11
12	$0.25T_{S_{13}}$	35.42	Reject	Frequency-selective	13	10, 11
13	$0.5T_{S_{13}}$	47.35	Reject	Frequency-selective	13	10, 11
14	$0.5T_{S_{13}}$	20.92	Reject	Frequency-selective	13	10, 11
15	$0.5T_{S_{13}}$	47.17	Reject	Frequency-selective	13	10, 11
16	$0.5T_{S_{13}}$	17.06	Reject	Frequency-selective	13	10, 11
17	$0.5T_{S_{12}}$	50.34	Reject	Frequency-selective	12	10
18	$0.5T_{S_{12}}$	38.75	Reject	Frequency-selective	12	10
19	$0.5T_{S_{12}}$	20.41	Reject	Frequency-selective	12	10
20	$0.5T_{S_{12}}$	22.66	Reject	Frequency-selective	12	10

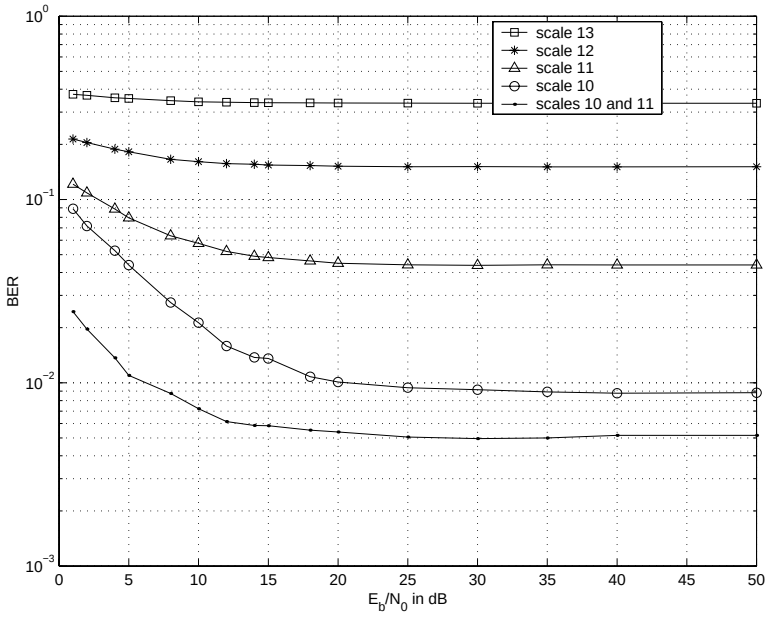

Figure 5.21: Bit Error Rate (BER) vs. E_b/N_0 in a frequency selective, slow fading channel with $f_d = 60$Hz and $\sigma_\tau = 30.5\mu s = 0.25T_{S_{13}}$. Improved BER performance is observed when both scales 10 and 11 are used.

Chapter 6

Conclusions

In this chapter we summarize and present conclusions based on the results in Chapter 5. Then we suggest some future areas for wavelet-based modulation research.

6.1 Conclusions

1. There was no appreciable difference between the Daubechies $N = 4$ and $N = 8$ wavelets. Both wavelets gave comparable performance in the AWGN and the flat fading channels.

2. WM performance is equivalent to BPSK in an AWGN channel for all scales. These results match Wornell's observation [19] and Ptasinki and Fellman's simulated results [10] for WM.

3. WM performance matches BPSK in a flat fading channel. A slight BER performance improvement exists at the higher scales. Also, WM performance in the 60Hz channel

was slightly better than in the 120Hz channel.

4. In the frequency-selective channel, the Doppler spread (60Hz and 120Hz) of the channel did not affect performance; instead, performance was limited by the ISI. When the rms delay spread was on the order of the bit period of a particular scale, the lower scales performed better (they experienced lower ISI). WM performed better than BPSK for scales 2 lower than the most corrupted scale.

5. A joint statistic significantly improved performance in all of the channels. In the AWGN channel, the WM improvement was commensurate with the improvement in a BPSK system with the same increase in signal energy (SNR). However, in the two fading channels, the improvements were larger than those in a BPSK system with the same increase in signal energy. In a BPSK system, the only way to realize the performance improvement is to boost SNR. In a WM system, you can listen longer or use a larger bandwidth. There are more choices with WM.

   (a) In the AWGN channel at $P_e = 10^{-5}$, an increase from 1 to 2 data copies resulted in a 3dB gain; an increase from 1 to 7 data copies resulted in an 8.47dB gain. Any combination of K noisy observations from any of the scales provided the same bit error rate.

   (b) In the flat fading channel ($f_d = 60Hz$) at $P_e = 10^{-4}$, an increase from 1 to 2 data copies resulted in an 18dB gain. An increase from 1 to 7 observations resulted in a 32dB gain. Any combination of scales used to generate the statistic showed approximately the same performance improvement.

   (c) In the frequency-selective channel, demodulation performance varied across scale—even for the joint statistic results. When scales with larger ISI were used in the joint statistic, the results were poor; however, when scales with low ISI were used, the results improved.

6. The multirate diversity of WM was used to successfully classify all three channel types

and estimate the rms delay spread for frequency-selective channels.

6.2 Directions for Future Work

The conclusions stated above suggest some avenues for future research.

1. The main disadvantage of WM is its bandwidth efficiency. Investigation of WM with higher order constellations and use of error control coding could lead to spectrally efficient, low error rate modulation schemes for WM.

2. Ptasinski and Fellman [10] showed that filtering of the mainlobe of the WM signal before transmission resulted in a more bandwidth efficient modulation scheme. The effectiveness of our new methods on this spectrally efficient filtered signal could be explored to see if current performance still holds good.

3. If the rms delay spread is of the order of the bit period of the highest transmitted scale, then the higher scales cannot be used for demodulation at the receiver. The use of equalization techniques at the receiver to compensate for this ISI would also make for interesting future research. If equalization is used, then the scales with large ISI offering higher data rates can be used. The higher scale demodulation would be useful when the channel was "open" only for a short time interval.

4. Wavelet modulation has a fixed time-frequency tiling diagram; it therefore cannot adapt to changing channel conditions. WPM, on the other hand, due to its flexible time-frequency tilings can adapt to changing channel conditions and would be highly resistant to jamming signals. This research initiative could be extended to implement wavelet packet modulation (WPM) in fading channels and jamming environments.

Bibliography

[1] R. H. Clarke. A statistical theory of mobile-radio reception. Bell Systems Technical Journal, 47:957–1000, 1968.

[2] Douglas Cochran and Chao Wei. A wavelet-based multiple-access spread spectrum modulation scheme. 13th Annual IEEE International Conference on Computers and Communications, pages 461–464, 1994.

[3] F. Daneshgaran and M. Mondin. Coded modulation and coherent frequency-hopped cdma with wavelets. Proceedings of MILCOM, pages 896–900, 1995.

[4] I. Daubechies. Ten Lectures on Wavelets. SIAM, Philadelphia, PA, first edition, 1992.

[5] Jay L. Devore. Probability & Statistics for Engineering and the Sciences. Brooks/Cole, Montery, California, first edition, 1982.

[6] M. J. Gans. A power spectral theory of propagation in the mobile radio environment. IEEE Transactions on Vehicular Technology, VT-21:27–38, 1972.

[7] S. G. Mallat. A theory for multiresolution signal decomposition: The wavelet representation. IEEE Transactions on Pattern Analysis and Machine Intelligence, 2(7):674–692, 1989.

[8] H. M. Newlin. Developments in the use of wavelets in communication systems. Proceedings of MILCOM, pages 343–349, 1998.

[9] John G. Proakis. Digital Communications. McGraw-Hill, New York, third edition, 1995.

[10] H. S. Ptasinski and R. D. Fellman. Implementation and simulation of a fractal modulation communication system. Proceedings of the IEEE SUPERCOMM/International Communications Conference, 3:1551–1555, 1994.

[11] H. S. Ptasinski and R. D. Fellman. Performance analysis of a fractal modulation communication system. Proceedings of the SPIE Wavelet Applications Conference, 2242:78–86, 1994.

[12] T. S. Rappaport. Wireless Communications. Prentice Hall, New Jersey, first edition, 1996.

[13] J. G. Proakis S. Srinidhi and M. Stojanovic. Wavelet based modulation for frequency hopped spread spectrum communications. 49th IEEE Vehicular Technology Conference, 2:904–908, 1999.

[14] Bernard Sklar. Rayleigh fading channels in mobile digital communication systems. IEEE Communications Magazine, 35(7):90–100, 1997.

[15] Scott Y. Siedel T. S. Rappaport and Rajendra Singh. 900-mhz multipath propagation measurements for u.s. digital cellular radiotelephone. IEEE Transactions on Vehicular Technology, 39(2):132–139, 1990.

[16] T.S. Rappaport Victor Fung and Berthold Thoma. Bit error simulation for $\pi/4$ dqpsk mobile radio communications using two-ray and measurement-based impulse response models. IEEE Transactions on Information Theory, 11(3):393–405, 1993.

[17] G. Bi W. Yang and T.P. Yum. A multirate wireless transmission system using wavelet packet modulation. 47th IEEE Vehicular Technology Conference, pages 368–372, 1997.

[18] G. W. Wornell. Signal Processing with Fractals: A Wavelet-Based Approach. Prentice Hall, New Jersey, first edition, 1996.

[19] G. W. Wornell and A. V. Oppenheim. Wavelet-based representations for a class of self-similar signals with application to fractal modulation. IEEE Transactions on Information Theory, 38(2):785–800, 1992.

[20] E. J. Yi and Edward J. Powers. Wavelet-based orthogonal modulation code. Proceedings of the 33rd Asilomar Conference on Signals, Systems and Computers, pages 674–692, 1999.

[21] C. Zarowski. Spectral characteristics and computation of wavelets for fractal modulation. Proceedings of the IEEE Pacific Rim Conference on Communications, Computers and Signal Processing, 2:370–373, 1993.

Vita

Manish J. Manglani was born on 15th December, 1973 in Bangalore, India. He studied at the Bangalore Institute of Technology, Bangalore, India where he earned his Bachelor's degree in telecommunication engineering. He then worked as a software research and development engineer with Siemens Communication Software Ltd. in Bangalore, India for a period of two years after which he enrolled in the Master's program in electrical engineering at Virginia Tech.

His academic interests include wireless communications and signal processing applications. His hobbies include hiking and biking. His favorite sport is tennis.